# Artemether prevents renal proximal tubules enlargement in high-fat diet induced obese mice

WENCI WENG[1], LINGLING SHEN[2], HONGHONG LIU[2], YATING ZHANG[1], XUEWEN YU[3], MUMIN SHAO[3], HUILI SUN[1] and PENGXUN HAN[1]

[1]Department of Nephrology, Shenzhen Traditional Chinese Medicine Hospital, The Fourth Clinical Medical College of Guangzhou University of Chinese Medicine, Shenzhen, Guangdong 518033, P.R. China; [2]Department of Nephrology, Shenzhen Traditional Chinese Medicine Hospital Affiliated to Nanjing University of Chinese Medicine, Shenzhen, Guangdong 518033, P.R. China; [3]Department of Pathology, Shenzhen Traditional Chinese Medicine Hospital, The Fourth Clinical Medical College of Guangzhou University of Chinese Medicine, Shenzhen, Guangdong 518033, P.R. China

Received July 14, 2026; Accepted October 19, 2026

DOI: 10.3892/mmr.2026.14067

**Abstract.** Enlarged kidney size is a common pathological manifestation in obesity, yet no effective therapeutic strategies currently exist to prevent this process. The present study aimed to investigate the effects of artemether, an artemisinin-based drug, on kidney weight and renal proximal tubules (PTs) enlargement in obese mice. High-fat diet (HFD)-induced obese mice were established and treated with artemether. Obesity phenotype, kidney weight and PTs pathology were evaluated. Molecular mechanisms were explored *in vitro* using TKPTS cells. The results demonstrated that artemether markedly reduced kidney weight and attenuated PTs enlargement in HFD mice independent of body weight changes. In HFD mice, PTs exhibited over-proliferation, excessive lipid droplets deposition and metabolic dysfunction. Artemether inhibited PTs hyperproliferation, reduced key glycolytic enzymes, upregulated mitochondrial pyruvate carrier (MPC) 1, MPC2 and isocitrate dehydrogenase subunit β in kidney. However, the renal triglyceride/cholesterol levels and mitochondrial β-oxidation related proteins were not affected by artemether. *In vitro*, artemether mitigated fatty acids-induced decline in mitochondrial membrane potential, modulated mitochondrial respiration and disturbed oxidative phosphorylation. Furthermore, although artemether decreased glycolytic gene transcription and glycolytic reserve, it unexpectedly increased lactate excretion. Additionally, artemether enhanced fatty acid oxidation, likely increased pyruvate oxidation and tricarboxylic acid cycle rate, and suppressed fatty acids activated TGF-β1 signaling. Collectively, these findings suggested that artemether reduces kidney weight and prevents PTs enlargement in HFD mice, likely through modulating mitochondrial respiration and remodeling energy metabolism.

*Correspondence to:* Dr Pengxun Han or Professor Huili Sun, Department of Nephrology, Shenzhen Traditional Chinese Medicine Hospital, The Fourth Clinical Medical College of Guangzhou University of Chinese Medicine, 1 Fuhua Road, Futian, Shenzhen, Guangdong 518033, P.R. China
E-mail: hpx2078@gzucm.edu.cn
E-mail: sunhuili2011@126.com

*Key words:* obesity, artemether, renal proximal tubule, mitochondria

## Introduction

Obesity stands as the most prevalent risk factor exacerbating kidney disease progression. The rising prevalence of obesity has made obesity-related kidney injury an increasingly common and notable public health challenge (1). Kidney enlargement is the typical early-stage pathological feature of obesity (2). Under normal physiological circumstances, kidney size maintains a relatively stable proportion to overall body mass. While moderate renal hypertrophy is regarded as a physiological adaptive response, excessive or disproportionate hypertrophy often indicates an underlying pathological process (3).

Previous studies reported that phosphatidylinositol 3-kinase signaling and lipid-regulated transcription factor PPARα serve a critical role in compensatory renal proximal tubules (PTs) growth after unilateral nephrectomy (4,5). In diabetic kidney disease, it is generally considered that PTs undergo initial proliferation and subsequent cellular hypertrophy in response to hyperglycemic stimulus, ultimately resulting in kidney hypertrophy (6). Multiple key signaling molecules, including TGF-β, mTOR and hypoxia-inducible factor, have been identified as critical mediators in driving this pathophysiological process (7). A previous study provided direct evidence that PTs proliferation, rather than cell hypertrophy, is responsible for kidney growth in both early type 1 and type 2 diabetes (8). In high-fat diet (HFD) induced obese mice, the kidneys became heavier and notable lipid droplet (LD) accumulation within renal tubules was observed (9). Previous studies demonstrated that insulin receptor activation, mitochondrial dysfunction, and autophagic stagnation are involved in HFD-induced PTs injury (10-12). However, the detailed mechanisms of PTs enlargement in HFD mice remains to be elucidated.

Artemether, a derivative of artemisinin, is a well-established antimalarial agent. It has been reported that artemisinin and its derivatives exhibit a variety of other biological activities, including antitumor, immune and metabolic regulatory properties (13). Our prior studies demonstrated that artemether can attenuate kidney injury in both type 1 and type 2 diabetic mouse models (14,15). The present study aimed to investigate the effects of artemether on PTs enlargement in HFD mice and to explore the underlying molecular mechanisms.

## Materials and methods

*Animals and treatments*. Male C57BL/6 mice (n=32; ~26 g; ~12 weeks old) were purchased from GemPharmatech Co., Ltd. and housed in the laboratory animal center at Peking University Shenzhen Graduate School (PKUSZ). All animal experiments were performed in accordance with the ARRIVE guidelines and approved by Animal Ethics Committee of PKUSZ (approval no. AP0044004). The mice were maintained at a controlled environment with temperature at 20-23˚C, relative humidity at 50-60%, a 12-h light/dark cycle and freely available food and water. At 3 months of age, the mice were allocated to normal diet (ND; n=8) or HFD (n=24) groups. ND (cat. no. 2112/2151; Beijing Keao Xieli Feed Co., Ltd.) energy supply ratio: Fat, 12.95%; protein, 24.02%; carbohydrate, 63.03%; 3.44 kcal/g. HFD (cat. no. D12492; Research Diets; BioPike LLC) energy supply ratio: Fat, 60%; protein, 20%; carbohydrate, 20%; 5.24 kcal/g. After 6 months (from 3 to 9 months of age) of HFD induction, 16 obese mice (body weight ≥50 g) were selected and allocated into the following HFD (n=8) and HFD + artemether (HFD + Art; n=8) groups. Mice in the HFD + Art group were fed HFD containing 2.0 g/kg artemether for 5 months (from 9-14 months of age).

*Cell culture*. The mouse kidney PT cell line (TKPTS; cat. no. CRL-3361) was obtained from American Type Culture Collection. The cells were maintained in a humidified incubator at 37˚C with 5% $CO_2$ and cultured in DMEM/F12 medium (Gibco; Thermo Fisher Scientific, Inc.; cat. no. 11330032) supplemented with 7% FBS (Gibco; Thermo Fisher Scientific, Inc.; cat. no. 10270106) and 5.57 $\mu$g/ml insulin (MilliporeSigma; cat. no. I9278). Various experiments were designed and implemented to elucidate the potential mechanisms.

Key reagents used in the present study are provided in Table I and sequences of the primers for reverse transcription-quantitative PCR (RT-qPCR) are provided in Table II.

*Physiological and metabolic parameters*. Body weight was recorded monthly. After the initiation of artemether treatment, 6 days per month were selected to monitor the food intake per mouse in each group. Fasting blood glucose was detected before and after artemether treatment with a blood glucose meter (Roche Diagnostics). The body composition before and after artemether treatment was analyzed using a nuclear magnetic resonance instrument (Suzhou Niumag Analytical Instrument Co., Ltd.; cat. no. QMR06-090H). Near the end of the experiment, the respiratory exchange ratio (RER) was measured utilizing the Comprehensive Lab Animal Monitoring System (CLAMS; Columbus Instruments).

*Tissue preparation*. After weighing the body weight, the mice were anesthetized with isoflurane (~3% for induction and 1~2% for maintenance), before drawing blood (~400 $\mu$l) from the orbital sinus vein. Afterwards, the mice were sacrificed by cervical dislocation. Mouse death was verified by cessation of heartbeat, respiratory arrest and pupil dilation. The kidney tissues were then isolated and weighed. Partial kidney tissues were fixed in 10% formalin at room temperature for ~48 h, dehydrated through a graded ethanol series, cleared in xylene, infiltrated with molten paraffin at ~60˚C and embedded in paraffin blocks. Some kidney tissues were embedded by OCT used for preparing frozen sections. Some renal cortex was cut into 1 $mm^3$ cubes used for preparing transmission electron microscope (TEM) ultrathin sections. The remaining kidney tissues were immediately snap-frozen in liquid nitrogen and stored at ultra-low temperature freezer. The concentrations of triglyceride (TG) and total cholesterol (TC) in renal tissue were determined according to the kit instructions. The serum TG and TC concentrations were measured by using an automatic biochemical analyzer (Roche Diagnostics).

*Histopathological analysis*. Frozen kidney sections (~10 $\mu$m) were stained with Oil red O at room temperature for 15 min to visualize the distribution of LD. Paraffin-embedded kidney sections (~3 $\mu$m) were stained with periodic acid-Schiff; (PAS) periodic acid solution for 10 min and Schiff reagent for 15 min at room temperature) and scanned by the Digital Slide Scanner (3DHistech Ltd.) for pathological analysis. A total of 20-30 proximal tubular areas and tubular lumen areas (axial ratio <1.5) in each section were measured. Number of nuclei in each proximal tubule was counted. The tubular wall area was calculated by subtracting the tubular lumen area from the renal tubular area. The images were analyzed using ImageJ software (version 1.8.0; National Institutes of Health) as previously described (16).

*Immunofluorescent staining*. Kidney tissue sections were deparaffinized and rehydrated. Following antigen retrieval using EDTA buffer, the sections were blocked with goat serum (Sangon Biotech Co., Ltd.) for 30 min at room temperature and then incubated overnight at 4˚C with primary antibodies against diacylglycerol O-acyltransferase (DGAT) 1 (1:100), mitochondrial pyruvate carrier (MPC) 2 (1:100), and isocitric dehydrogenase subunit β (IDH3B; 1:100). The phosphate buffered saline (PBS) was used as the washing buffer, with three washes performed between each step. After mixing FITC-conjugated lotus tetragonolobus lectin (LTL) (5 $\mu$g/ml), DAPI (0.5 $\mu$g/ml) and the appropriate Alexa Fluor-conjugated secondary antibodies (all 1:500), the sections were incubated with the mixture for 1 h at 37˚C. Co-stained sections were visualized and imaged using a confocal microscope (LSM710; Carl Zeiss AG).

*TEM*. The small renal cortex cubes were fixed in 2.5% glutaraldehyde for ~48 h at 4˚C, followed by post-fixation in 1% osmic acid for ~1.5 h at room temperature. After dehydration through a graded ethanol series, samples were infiltrated with and embedded in epoxy resin. The resin blocks were polymerized at 40˚C overnight and subsequently at 60˚C for 48 h. Ultrathin sections (70-80 nm) were cut, collected on

Table I. Key reagents used in this study.

| Reagent | Source | Catalogue number |
|---|---|---|
| Artemether | ConBon Bio-technology | CB-NA-8052 |
| PAS staining kit | Beijing Solarbio Science & Technology Co., Ltd. | G1281 |
| Oil red O staining kit | Beijing Solarbio Science & Technology Co., Ltd. | G1261 |
| TG content assay kit | Beijing Solarbio Science & Technology Co., Ltd. | BC0625 |
| TC content assay kit | Beijing Solarbio Science & Technology Co., Ltd. | BC1985 |
| Goat serum | Sangon Biotech Co., Ltd. | E510009-0100 |
| Lotus tetragonolobus lectin fluorescein (FITC) | Thermo Fisher Scientific, Inc. | L32480 |
| Goat anti-Rabbit Secondary antibody, Alexa Fluor™ 594 | Thermo Fisher Scientific, Inc. | A11037 |
| Goat anti-Mouse Secondary antibody, Alexa Fluor™ 594 | Thermo Fisher Scientific, Inc. | A11032 |
| DAPI | MilliporeSigma | D9542 |
| DGAT1 antibody | Proteintech Group, Inc. | 11561 |
| CPT1A antibody | Proteintech Group, Inc. | 15184 |
| CPT2 antibody | Proteintech Group, Inc. | 26555 |
| ACADVL antibody | Proteintech Group, Inc. | 14527 |
| ACADL antibody | Proteintech Group, Inc. | 17526 |
| ACADM antibody | Proteintech Group, Inc. | 55210 |
| ACADS antibody | Proteintech Group, Inc. | 16623 |
| HK2 antibody | Proteintech Group, Inc. | 22029 |
| PFKM antibody | Proteintech Group, Inc. | 55028 |
| PKM antibody | Proteintech Group, Inc. | 10078 |
| MPC1 antibody | Novus Biologicals | NBP1-91706 |
| MPC2 antibody | Proteintech Group, Inc. | 20049 |
| CS antibody | Proteintech Group, Inc. | 16131 |
| ACO2 antibody | Proteintech Group, Inc. | 11134 |
| IDH3B antibody | Proteintech Group, Inc. | 68199 |
| ACLY antibody | Proteintech Group, Inc. | 15421 |
| ACSS2 antibody | Proteintech Group, Inc. | 16087 |
| β-actin antibody | MilliporeSigma | A5441 |
| Anti-rabbit IgG-HRP antibody | Thermo Fisher Scientific, Inc. | 65-6120 |
| Anti-mouse IgG-HRP antibody | Thermo Fisher Scientific, Inc. | 62-6520 |
| PureLink™ RNA mini kit | Thermo Fisher Scientific, Inc. | 12183018A |
| $Oligo(dT)_{12-18}$ Primers | Thermo Fisher Scientific, Inc. | 18418012 |
| dNTP Mix | Thermo Fisher Scientific, Inc. | 18427013 |
| RNaseOUT™ Ribonuclease Inhibitor | Thermo Fisher Scientific, Inc. | 10777019 |
| M-MLV Reverse Transcriptase | Thermo Fisher Scientific, Inc. | 28025013 |
| SYBR green PCR master mix | Thermo Fisher Scientific, Inc. | 4367659 |
| BSA Control for BSA-Fatty Acid Complexes | Cayman Chemical Company | 29556 |
| BSA-Palmitate Saturated Fatty Acid Complex | Cayman Chemical Company | 29558 |
| BSA-Oleate Monounsaturated Fatty Acid Complex | Cayman Chemical Company | 29557 |
| JC-1 Mitochondrial Membrane Potential Assay Kit | MedChemExpress | HY-K0601 |
| MT-1 MitoMP Detection Kit | Dojindo Laboratories, Inc. | MT13 |
| Seahorse XF Cell Mito Stress Test Kit | Agilent Technologies, Inc. | 103015-100 |
| Seahorse XF Glycolysis Stress Test Kit | Agilent Technologies, Inc. | 103020-100 |
| Glycolysis Assay Kit | MilliporeSigma | MAK439 |
| ATP Synthase Activity Assay Kit | Wuhan Elabscience Biotechnology Co., Ltd. | E-BC-K838-M |
| Cytochrome c Oxidase Activity Assay Kit | Wuhan Elabscience Biotechnology Co., Ltd. | E-BC-K837-M |

Table I. Continued.

| Reagent | Source | Catalogue number |
|---|---|---|
| Mitochondrial Complex II Activity Assay Kit | Wuhan Elabscience Biotechnology Co., Ltd. | E-BC-K835-M |
| Fatty Acid Oxidation (FAO) Colorimetric Assay Kit | Wuhan Elabscience Biotechnology Co., Ltd. | E-BC-K784-M |

PAS, periodic acid-Schiff; TG, triglyceride; TC, total cholesterol; DGAT1, diacylglycerol O-acyltransferase 1; CPT1A, carnitine palmitoyltransferase 1A; CPT2, carnitine palmitoyltransferase 2; ACAD, acyl-CoA dehydrogenase; ACADVL, ACAD very long chain; ACADL, ACAD long chain; ACADM, ACAD medium chain; ACADS, ACAD short chain; HK2, hexokinase 2; PFKM, phosphofructokinase, muscle; PKM, pyruvate kinase, muscle; MPC1, mitochondrial pyruvate carrier 1; MPC2, mitochondrial pyruvate carrier 2; CS, citrate synthase; ACO2, aconitase 2; IDH3B, isocitric dehydrogenase subunit β; ACLY, ATP citrate lyase; ACSS2, acyl-CoA synthetase short chain family member 2; BSA, bovine serum albumin.

Table II. Sequences of the primers for reverse transcription-quantitative PCR.

| Gene | Primer sequence (5'-3') |
|---|---|
| Mouse *Ki-67* | Forward: ATCATTGACCGCTCCTTTAGGT |
| | Reverse: GCTCGCCTTGATGGTTCCT |
| Mouse *Tgfb1* | Forward: CCGCAACAACGCCATCTATG |
| | Reverse: CTCTGCACGGGACAGCAAT |
| Mouse *Tgfbr1* | Forward: TCTGCATTGCACTTATGCTGA |
| | Reverse: AAAGGGCGATCTAGTGATGGA |
| Mouse *Tgfbr2* | Forward: CCGCTGCATATCGTCCTGTG |
| | Reverse: AGTGGATGGATGGTCCTATTACA |
| Mouse *Atgl* | Forward: GGATGGCGGCATTTCAGACA |
| | Reverse: CAAAGGGTTGGGTTGGTTCAG |
| Mouse *Mpc1* | Forward: GGTACAACCTCGAAACTGG |
| | Reverse: TCAAGAGCTGGTCCTTGTACC |
| Mouse *Mpc2* | Forward: TACCACCGACTCATGGATAAAGT |
| | Reverse: CACACACCAATCCCCATTTCA |
| Mouse *Idh3b* | Forward: TGGAGAGGTCTCGGAACATCT |
| | Reverse: AGCCTTGAACACTTCCTTGAC |
| Mouse *Dgat1* | Forward: CCCATACCCGGGACAAAGAC |
| | Reverse: ATCAGCATCACCACACACCA |
| Mouse *Dgat2* | Forward: GCGCTACTTCCGAGACTACTT |
| | Reverse: GGGCCTTATGCCAGGAAACT |
| Mouse *β-actin* | Forward: GGACTCCTATGTGGGTGACG |
| | Reverse: AGGTGTGGTGCCAGATCTTC |

copper grids, and sequentially stained with uranyl acetate (8 min at room temperature) and lead citrate (8 min at room temperature) to enhance ultrastructural contrast. The sections were examined using a JEM-1400 transmission electron microscope (JEOL, Ltd.). In each group, renal tubules fields containing LD were selected and imaged, and then the images were processed using ImageJ software (Version 1.8.0; National Institutes of Health).

*Western blotting analysis*. Renal tissues were homogenized and prepared in sample loading buffer (Bio-Rad Laboratories, Inc.). The protein concentrations were determined using Bradford Dye Reagent (Bio-Rad Laboratories, Inc.). The same mass of protein (~15 $\mu$l/45 $\mu$g) was loaded per lane. The homogenates were separated on SDS-PAGE gels (10%) and transferred to PVDF membranes (Merck KGaA). After blocking in 5% non-fat milk for 1 h at room temperature, the membranes were incubated overnight at 4˚C with the following primary antibodies: Carnitine palmitoyltransferase (CPT) 1A (1:500), CPT2 (1:500), acyl-CoA dehydrogenase (ACAD) very long chain (ACADVL; 1:500), ACAD long chain (ACADL; 1:500), ACAD medium chain (ACADM; 1:500), ACAD short chain (ACADS; 1:500), Hexokinase 2 (HK2; 1:500), Phosphofructokinase, muscle

(PFKM; 1:500), Pyruvate kinase, muscle (PKM; 1:500), MPC1 (1:500), MPC2 (1:500), Citrate synthase (CS; 1:500), Aconitase 2 (ACO2; (1:500), IDH3B (1:500), ATP citrate lyase (ACLY; 1:500), acyl-CoA synthetase short chain family member 2 (ACSS2; 1:500) and β-actin (1:2,000). Then the membranes were incubated with appropriate secondary antibodies (cat. nos. 65-6120/Anti-rabbit IgG-HRP antibody or 62-6520/Anti-mouse IgG-HRP antibody; Thermo Fisher Scientific, Inc. both 1:2,000) and detected using the ChemiDoc Imaging System (Bio-Rad Laboratories, Inc.). The densitometry was analyzed using ImageJ software (Version 1.8.0; National Institutes of Health). β-actin was used as a loading control.

*RT-qPCR*. Total RNA was extracted using the PureLink™ RNA mini kit. The first-strand cDNA was synthesized using Oligo(dT)$_{12-18}$ Primers, dNTP Mix, RNaseOUT™ Ribonuclease Inhibitor and M-MLV Reverse Transcriptase. Renal tissue (~20 mg) was harvested for total RNA extraction. The RNA extraction, cDNA synthesis, and qPCR were performed according to the manufacturer's protocols. The reaction process was under 37˚C for 50 min and then was terminated at 70˚C for 15 min. qPCR was performed using SYBR green PCR master mix by the Applied Biosystems QuantStudio 5 platform and the amplification conditions (95˚C for 5 min followed by 45 cycles of 95˚C for 15 sec, 55˚C for 15 sec, and 72˚C for 20 sec) were set as previously described (17). Gene-specific primers were synthesized by Sangon Biotech Co., Ltd. The relative RNA expression levels were calculated using $2^{-\Delta\Delta Cq}$ and normalized against the housekeeping gene *beta-actin* (18).

*Mitochondrial membrane potential (MMP) assay (JC-1 Staining)*. JC-1 staining for MMP analysis was performed according to a previously published bio-protocol (19). The TKPTS cells (1x10$^5$ cells per well) were seeded into 6-well plates and cultured overnight. The experimental groups were designed as follows (n=6 per group): Bovine serum albumin (BSA; 0.25 mM), BSA + Art (0.25 mM + 300 $\mu$M), palmitic acid (PA; 0.25 mM), PA + Art (0.25 mM + 300 $\mu$M), oleic acid (OA; 0.25 mM), OA + Art (0.25 mM + 300 $\mu$M), PA + OA (0.25 mM + 0.25 mM), PA + OA + Art (0.25 mM + 0.25 mM + 300 $\mu$M) and BSA + Carbonyl cyanide 3-chlorophenylhydrazone (CCCP; 0.25 mM + 16.7 $\mu$M). The cells were then switched to pre-prepared medium containing the designed components and cultured for 6 h at 37˚C. The BSA + CCCP positive control group cells were exposed to 16.7 $\mu$M CCCP for 5 min at 37˚C. Subsequently, all wells were incubated with 10 $\mu$l of JC-1 dye (2 $\mu$M final concentration) for 30 min at 37˚C. After staining, the supernatant was aspirated, and the cells were washed twice with phosphate-buffered saline (PBS) and resuspended in ~400 $\mu$l of PBS. Subsequently, 100 $\mu$l cell resuspension solution from each well was added into a black 96-well plate. Fluorescence intensity was measured using a microplate reader (Synergy H1; BioTek; Agilent Technologies, Inc.), with red and green fluorescence detected at excitation/emission wavelengths of 550/600 and 485/535 nm, respectively. The red/green fluorescence ratio was then calculated and used to represent changes in MMP.

*MT-1 staining*. The TKPTS cells (1x10$^5$ cells per well) were seeded into 6-well plates and cultured overnight. When ~70% confluence was reached, cells were treated with medium containing BSA (0.5 mM), PA + OA (0.25 mM + 0.25 mM) or PA + OA + Art (0.25 mM + 0.25 mM + 300 $\mu$M) for 6 h at 37˚C. The cells were stained with MT-1 according to the manufacturer's protocol and imaged using confocal microscopy (LSM710; Carl Zeiss AG). In each group, 10 fields at x20 objective were selected to calculate the mean fluorescence intensity values. CCCP intervention for 5 min was performed as a positive control (BSA + CCCP, 0.5 mM + 16.7 $\mu$M).

*Cell mito stress test and glycolysis stress test*. TKPTS cells (60x10$^3$ cells per well) were seeded into a Seahorse XFe24 cell culture plate (Agilent Technologies, Inc.) and cultured for 24 h. Prior to the experiment, the assay medium was supplemented with the indicated concentrations of BSA (0.2 mM), PA (0.2 mM), OA (0.2 mM), PA + Art (0.2 mM + 300 $\mu$M) or OA + Art (0.2 mM + 300 $\mu$M). The experimental procedure was then carried out in accordance with the manufacturer's protocol using the Seahorse XFe24 analyzer (Agilent Technologies, Inc.).

*Cell ATP synthase activity and glycolysis (lactate excretion in cell media) assay*. TKPTS cells (1x10$^5$ cells per well) were seeded into 6-well plates and cultured for 24 h at 37˚C. After washing with PBS, the cells were treated with media (2.0 ml) containing BSA (0.5 mM), PA + OA (0.25 mM + 0.25 mM) and PA + OA + Art (0.25 mM + 0.25 mM + 300 $\mu$M) for 24 h at 37˚C. Subsequently, the cell media in each group were collected and used for lactate determination. The cells were collected and used for cell mitochondrial ATP synthase activity assay. A total of four independent experiments were performed in each group.

*Cytochrome c oxidase, mitochondrial Complex II and fatty acid oxidation activity assay*. The cell culture and intervention protocols were identical to those used for the ATP synthase activity assay. Cells from each group were harvested and processed in accordance with the manufacturer's instructions (Wuhan Elabscience Biotechnology Co., Ltd.).

*RNA sequencing (RNA-seq)*. Cell culture and intervention procedures were same to those used for the ATP synthase activity assay. Total RNA was extracted from cells in each group and sent to Sangon Biotech Co., Ltd. for RNA-seq and subsequent analysis. The heatmaps were generated from transcripts per million (TPM) data to visually represent the relative expression levels of genes across the different experimental groups. RNA sequencing datasets are available in the Gene Expression Omnibus database at accession no. GSE317009 (https://www.ncbi.nlm.nih.gov/geo/query/acc.cgi?&acc=GSE317009).

*Statistical analysis*. Data are presented as the mean ± standard deviation. Data analysis was performed using SPSS software (Version 22.0; IBM Corp.). One-way analysis of variance followed by LSD post hoc test was used for data analysis; Bonferroni post hoc test was used for JC-1 and MT-1 (groups >3) data analysis. $P<0.05$ was considered to indicate a statistically significant difference.

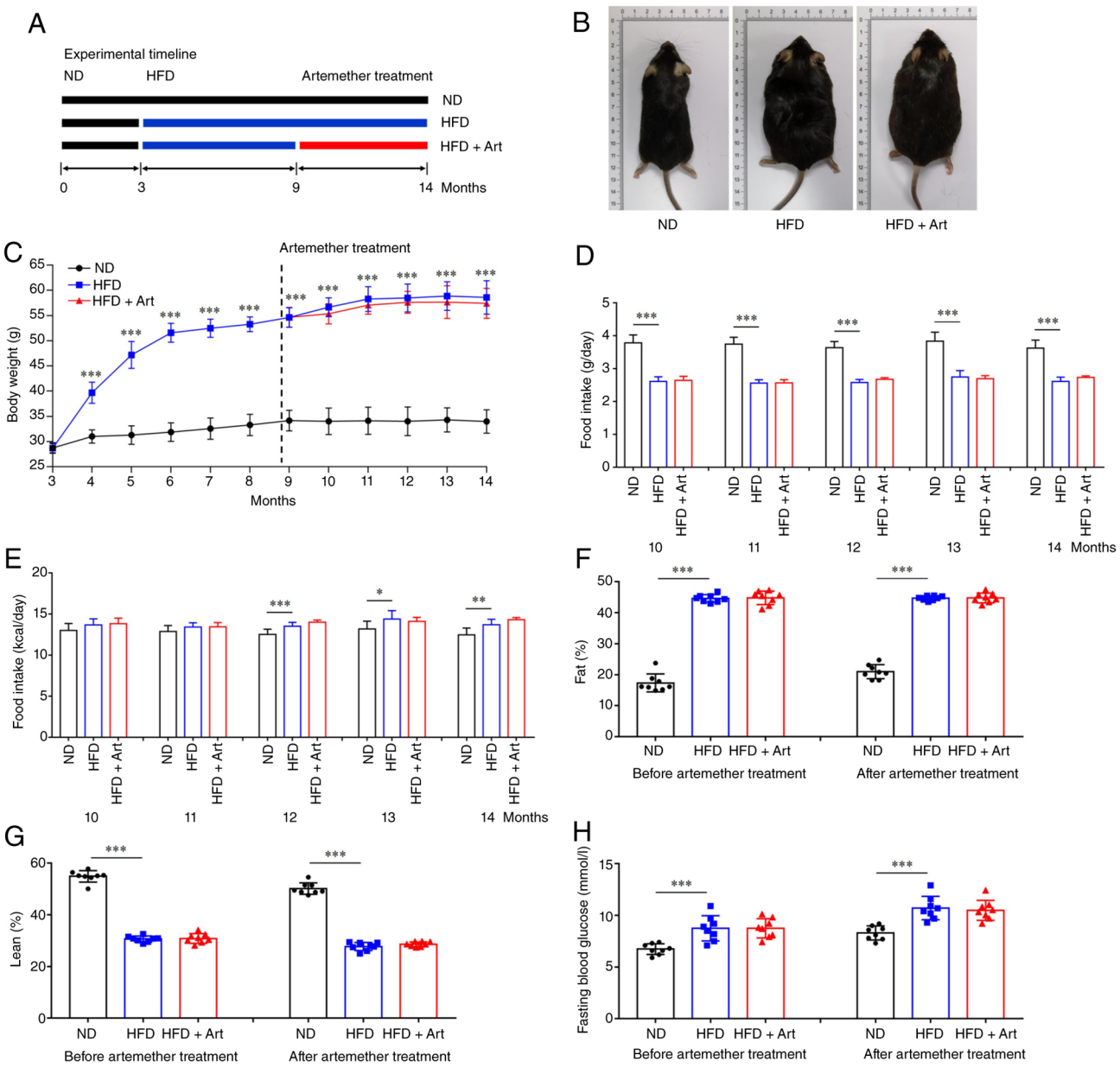



Figure 1. Effects of artemether on body weight, food intake, body composition and fasting blood glucose in long-term HFD induced obese mice. (A) Schematic depicting the experimental design and timeline. (B) Representative photographs of mice from each group prior to study termination. (C) Longitudinal body weight changes in the three experimental groups (during the 3-8 month period: ND group, n=8; HFD group, n=24; during the 9 to 14 month period: n=8 per group). Average food intake per mouse was quantified monthly, expressed as (D) mass (g/day) and (E) calculated by calorie (kcal/day) for each group after artemether administration. Body composition analysis showing (F) fat and (G) lean ratio for each group before and after artemether intervention. (H) Fasting blood glucose levels across the three groups before and after artemether treatment. n=8 per group. $^{*}$P<0.05, $^{**}$P<0.01, and $^{***}$P<0.001 vs. the ND group. HFD, high-fat diet; ND, normal diet.

## Results

*Artemether treatment has no significant impact on body weight, food intake, body composition and fasting blood glucose in long-term HFD-induced obese mice.* The experimental timeline diagram (Fig. 1A) illustrates the key events in the present study. Representative mouse images from each group at the end of the experiment are shown in Fig. 1B. Compared with the ND group, the body weight in the HFD group mice increased rapidly in the first 3 months (from 3 to 6 months of age) and then weight gain slowed down in the following period (Fig. 1C). Artemether treatment for 5 months (from 9 to 14 months of age) had no significant impact on body weight (Fig. 1C). Taking into account the influence of dietary intake on body weight, the average food intake in each group was monitored during the artemether intervention period. As shown in Fig. 1D, the HFD group consumed markedly less food by mass (g/day) than the ND group. However, when measured in calories (kcal/day), food intake was higher in the HFD group, particularly in the last 3 months (Fig. 1E). Notably, no significant difference was observed between the HFD and HFD + Art groups during the treatment period (Fig. 1D and E). Regarding body composition and fasting blood glucose, the HFD group displayed a

distinct obese phenotype (higher fat ratio and lower lean ratio) and abnormally elevated fasting blood glucose levels both before and after artemether treatment (Fig. 1F-H). However, artemether intervention had no significant impact on these parameters (Fig. 1F-H).

*Without affecting body weight, artemether reduces kidney weight, prevents PTs enlargement and proliferation, and regulates Tgfb1 signal pathway in HFD mice*. Compared with the ND group, the kidneys of the HFD group became markedly heavier after long-term HFD and the pathological change was markedly ameliorated by artemether (Fig. 2A, C and D). The PTs serve a pivotal role in kidney function and constitute the majority of the renal parenchyma. In the HFD group mice, enlarged proximal tubular area, proximal tubular wall area and proximal tubular lumen area were detected (Fig. 2B and E-G). Additionally, an abnormally increased number of nuclei per PT and markedly upregulated mRNA levels of *Ki-67* (a proliferation marker) in renal tissue were also observed in the HFD group (Fig. 2H and I). Artemether treatment markedly prevented PTs enlargement, reduced nuclei count per PT, and downregulated *Ki-67* expression (Fig. 2B and E-I). TGF-β1 serves an important role in the injury and proliferation of PTs. In the HFD group, a significant elevation in the mRNA levels of *Tgfb1* and TGF-β receptor 1 (*Tgfbr1*) were observed, along with a mild increase in *Tgfbr2* mRNA expression (Fig. 2J-L). Artemether had no significant effect on *Tgfb1* mRNA levels, but it notably suppressed *Tgfbr1* and *Tgfbr2* mRNA expression (Fig. 2J-L).

*PTs are the prominent sites of LD accumulation within the kidney*. After prolonged HFD induction, renal tissue exhibited markedly elevated TG and TC levels, which were not affected by artemether treatment (Fig. 3A and B). As shown in Fig. 3C, the Oil red O staining of kidney frozen sections revealed mild LD deposition within renal tubules in the ND group, which was markedly exacerbated following the HFD. TEM images from each group further corroborated these changes in LD deposition within renal tubules (Fig. 3D). The co-staining of DGAT1 (an LD-associated protein) and LTL (a brush border marker for PTs) showed that PTs are the areas where LDs accumulate (Fig. 3E).

*Comparative analysis of the RER, mitochondrial β-oxidation related proteins and adipose triglyceride lipase (Atgl) mRNA levels among the three groups*. RER is a key indicator for assessing metabolic fuel utilization. Compared with the ND group, HFD group mice exhibited a loss of RER circadian rhythm and markedly lower RER values, indicating a systemic shift toward fatty acid oxidation as the main energy source (Fig. 4A and B). Mitochondrial β-oxidation is the primary pathway for fatty acid degradation and cellular energy production. CPT1A, CPT2, ACADVL, ACADL, ACADM and ACADS are important proteins regulating this process (20). Among the three groups, no significant differences of these protein levels were detected by western blotting (Fig. 4C and D). However, the markedly downregulated mRNA levels of *Atgl* in renal tissue suggested impaired TG lipolysis in kidney after HFD induction (Fig. 4E). Artemether intervention further reduced RER values during both the dark (active) and light (inactive) phases (Fig. 4A and B). Notably, artemether also markedly upregulated *Atgl* mRNA expression in renal tissue (Fig. 4E).

*Artemether treatment downregulates key glycolytic enzymes and upregulates MPC1 and MPC2 expression*. Although fatty acid oxidation serves as the primary energy source in renal tubules, the glycolysis pathway also serves an important role and cannot be ignored (21). HK2, PFKM and PKM are the key enzymes in glycolysis. As illustrated in Fig. 5A-D, no significant differences of these proteins were detected between the ND group and the HFD group. MPC is the essential mitochondrial inner membrane protein that mediates the uptake of pyruvate into mitochondrial matrix (22). Compared with the ND group, significant reductions of the protein and mRNA expression levels of *Mpc1* and *Mpc2* were detected in the HFD group (Fig. 5A and E-H). Treatment with artemether led to a significant decrease in the protein levels of HK2, PFKM, and PKM (Fig. 5A-D). Meanwhile, the protein and mRNA expression levels of *Mpc1* and *Mpc2* were markedly upregulated by artemether (Fig. 5A and E-H). To identify the specific renal tubular sites where these metabolic changes occur, a co-staining experiment of MPC2 and LTL was performed. The co-staining images revealed that MPC2 expression was highly co-localized with LTL, and the fluorescence intensity patterns were consistent with the western blotting results (Fig. 5I).

*Artemether upregulates Idh3b expression, a key enzyme controlling the tricarboxylic acid (TCA) cycle*. The TCA cycle, also known as the citric acid cycle, is the key metabolic pathway that connects carbohydrate, fat and protein metabolism (23). CS, ACO2 and IDH3B are the main enzymes regulating citrate synthesis and isocitrate dehydrogenation activity. No significant changes in the protein levels of these enzymes were observed between the ND and HFD groups (Fig. 6A-D). ACLY and ACSS2 are cytoplasmic acetyl-CoA synthetases that utilize citrate and acetate, respectively, as their reaction substrates (24). The HFD group showed markedly increased ACLY protein levels and decreased ACSS2 protein levels (Fig. 6A, E and F), suggesting that cytoplasmic acetyl-CoA synthesis predominantly relied on citrate in this group. After artemether treatment, both the protein and mRNA levels of *Idh3b* were markedly upregulated (Fig. 6A, D and G), while no marked changes were observed in the other proteins (Fig. 6A-C, E and F). To further investigate whether PTs are the site of artemether action, co-staining of IDH3B and LTL was performed. As shown in Fig. 6H, IDH3B was widely expressed in renal tubules, with partial co-localization observed with LTL.

The *in vivo* animal experimental results from the present study suggested that artemether's biological effect in attenuating PTs enlargement is also closely linked to mitochondrial metabolism. To further clarify the underlying mechanisms, subsequent *in vitro* experiments were performed using TKPTS cells.

*Artemether mitigates fatty acid-induced MMP decline in TKPTS cells*. MMP is crucial for cellular energy conversion and can be assessed using fluorescent probes such as JC-1 and MT-1 (25). When employing the JC-1 fluorescence detection method (19), a significant reduction in MMP in TKPTS cells was observed following 6-h treatment with PA, OA or

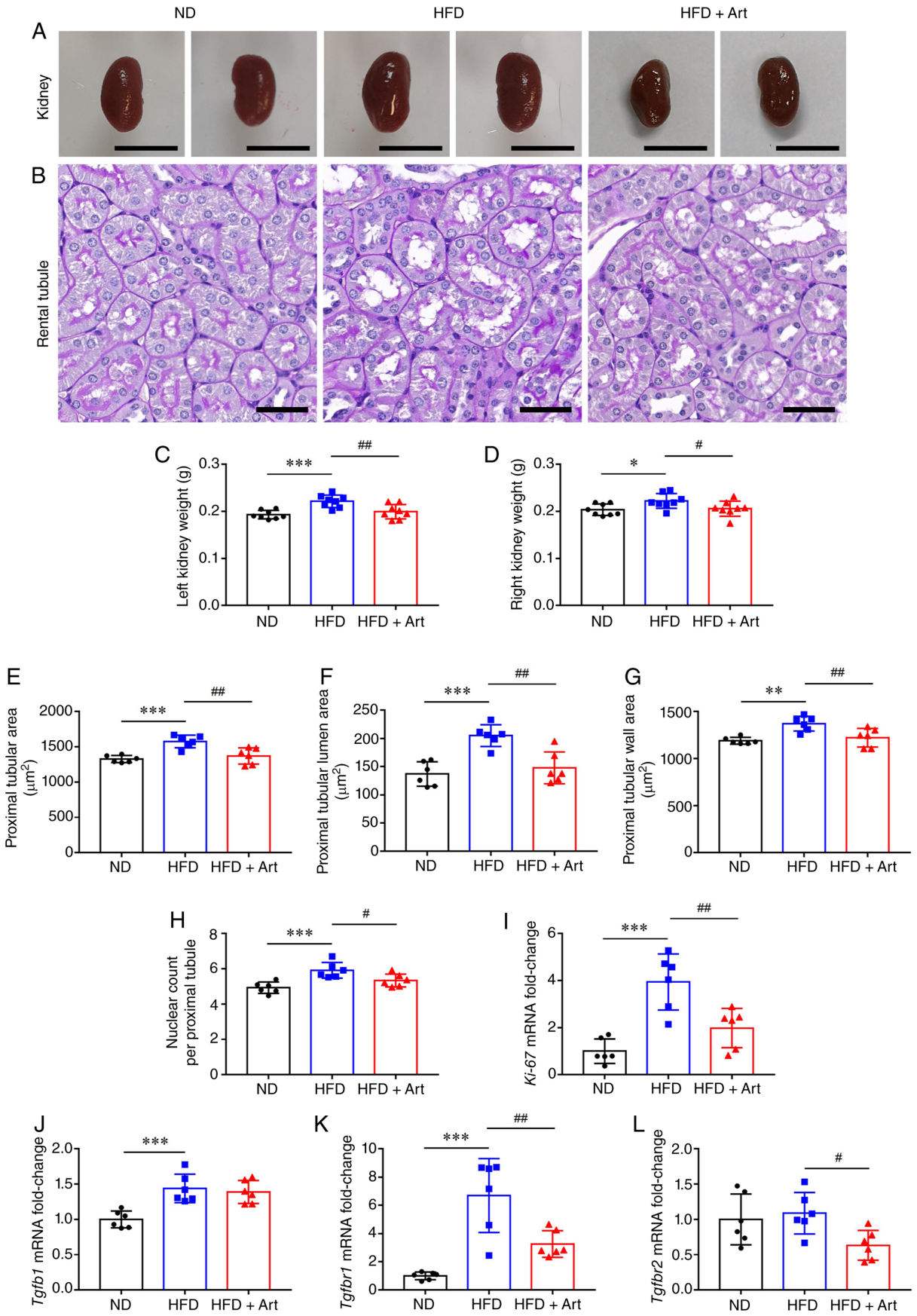



Figure 2. Artemether reduces kidney weight, inhibits PTs enlargement and proliferation, downregulates *Ki-67* mRNA expression, and regulates TGF-β1 signaling in HFD mice. (A) Representative kidney images from each experimental group. Scale bars, 1 cm. (B) PAS staining of renal tubule. Scale bars, 40 $\mu$m. (C) Left and (D) right kidney weights in each group at the end of the experiment. n=8 per group. Bar graphs showing the (E) proximal tubular area, (F) tubular lumen area and (G) tubular wall area in the three groups. (H) Number of nuclei per proximal tubule across the three groups. Relative mRNA expression levels of (I) *Ki-67*, (J) *Tgfb1*, (K) *Tgfbr1* and (L) *Tgfbr2* in renal tissue across the three groups. n=6 per group. $^{*}$P<0.05, $^{**}$P<0.01, and $^{***}$P<0.001 vs. the ND group; $^{\#}$P<0.05 and $^{\#\#}$P<0.01 vs. the HFD group. PAS, periodic acid-Schiff; PTs, proximal tubules; *Tgfbr*, TGF-β receptor; HFD, high-fat diet; ND, normal diet; Art, artemether.

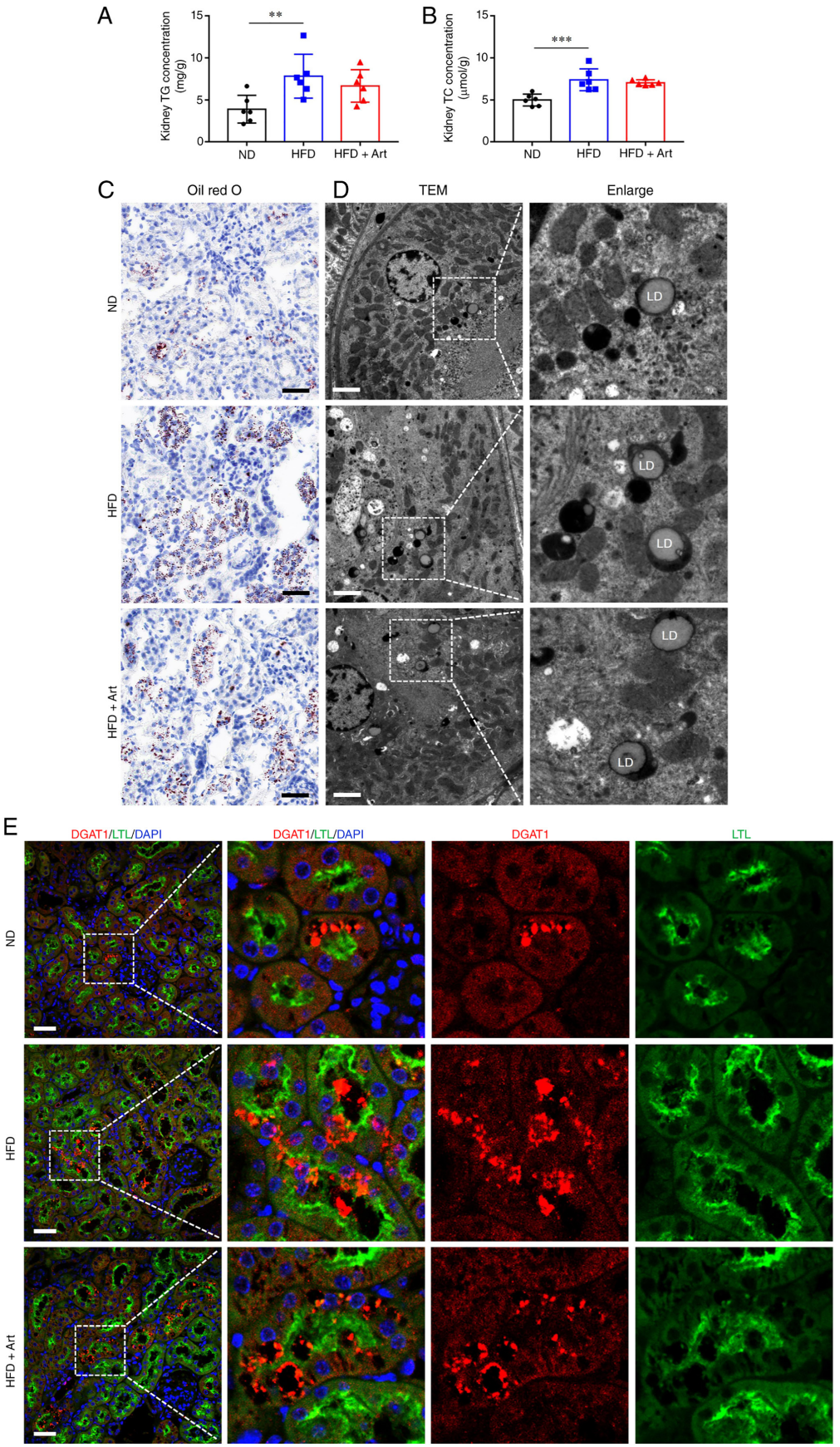



Figure 3. Determination of TG and TC levels in renal tissue, and analysis of lipid droplet distribution within renal tubules. Bar graphs depicting renal (A) TG and (B) TC concentrations across the three groups. n=6 per group. $^{**}$P<0.01 and $^{***}$P<0.001 vs. the ND group. (C) Kidney frozen sections stained with Oil red O. Scale bars, 40 $\mu$m. (D) Representative transmission electron microscopy images showing lipid droplet deposition within renal tubules. Scale bars, 2 $\mu$m. (E) Representative fluorescence images of kidney paraffin sections co-stained for DGAT1 (a lipid droplet-associated protein) and LTL (a brush border marker for proximal tubules). Scale bars, 40 $\mu$m. TG, triglyceride; TC, total cholesterol; ND, normal diet; HFD, high-fat diet; DGAT1, diacylglycerol O-acyltransferase 1; LTL, lotus tetragonolobus lectin; TEM, transmission electron microscope; LD, lipid droplet; Art, artemether.

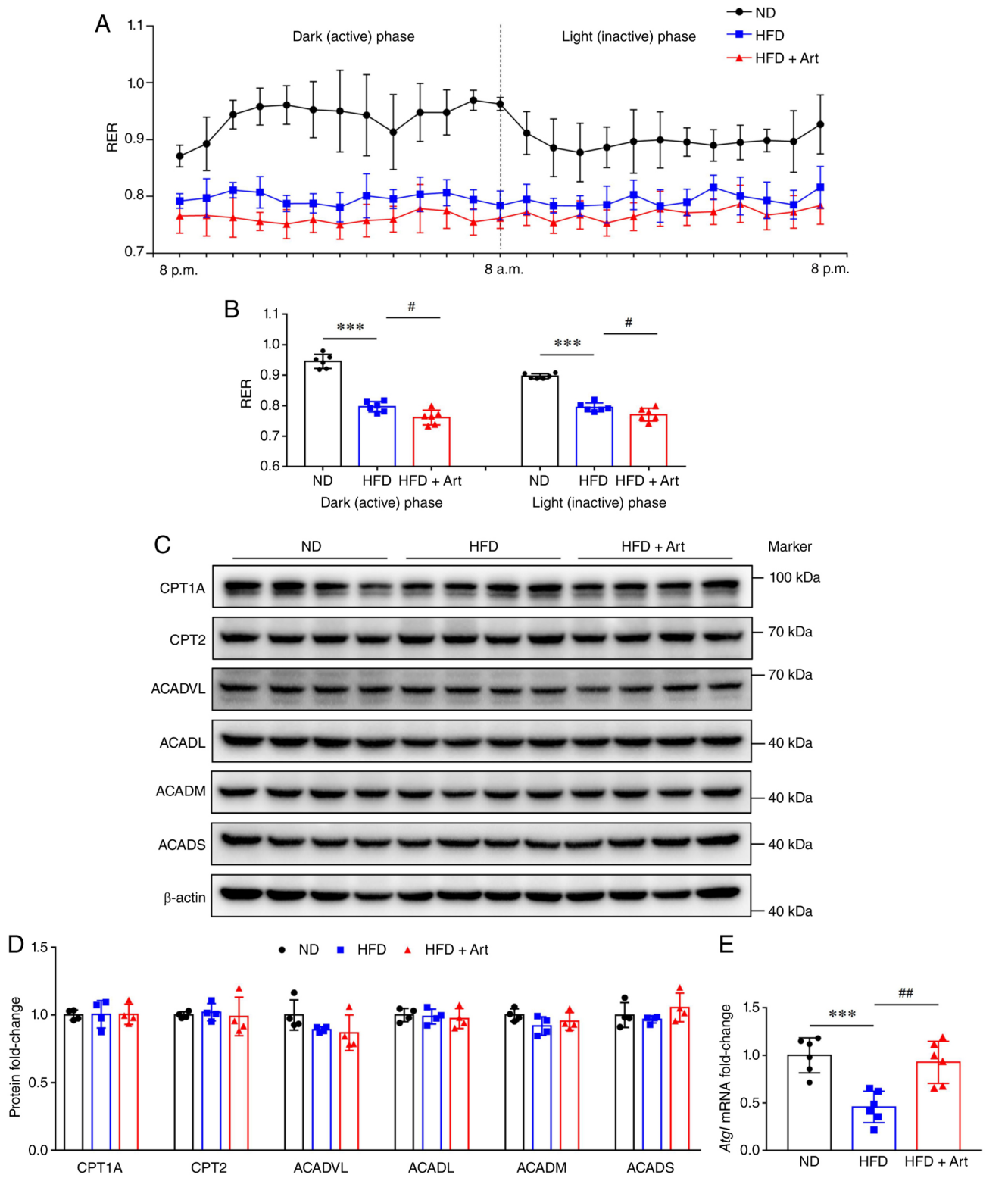



Figure 4. Alterations in RER values, mitochondrial β-oxidation related proteins and *Atgl* mRNA levels. (A) Time course of RER values for each group over 24 h, and (B) average RER values during the dark (active) and light (inactive) phases. n=6 per group. (C) Representative immunoblots and (D) corresponding quantification of CPT1A, CPT2, ACADVL, ACADL, ACADM and ACADS protein levels in renal tissue across the three groups. n=4 per group. (E) *Atgl* mRNA expression levels in renal tissue among the three groups. n=6 per group. $^{***}$P<0.001 vs. the ND group; $^{\#}$P<0.05 and $^{\#\#}$P<0.01 vs. the HFD group. RER, respiratory exchange ratio; *Atgl*, adipose triglyceride lipase; CPT, carnitine palmitoyltransferase; ACAD, acyl-CoA dehydrogenase; ACADVL, ACAD very long chain; ACADL, ACAD long chain; ACADM, ACAD medium chain; ACADS, ACAD short chain; ND, normal diet; HFD, high-fat diet; Art, artemether.

their combination (PA + OA). Notably, artemether effectively mitigated the fatty acid induced decline in MMP but had no significant effect on the BSA control group (Fig. 7A). To further validate this regulating effect of artemether, MMP was measured in adherent cells treated with PA + OA using the MT-1 fluorescent dye. Compared with the BSA control

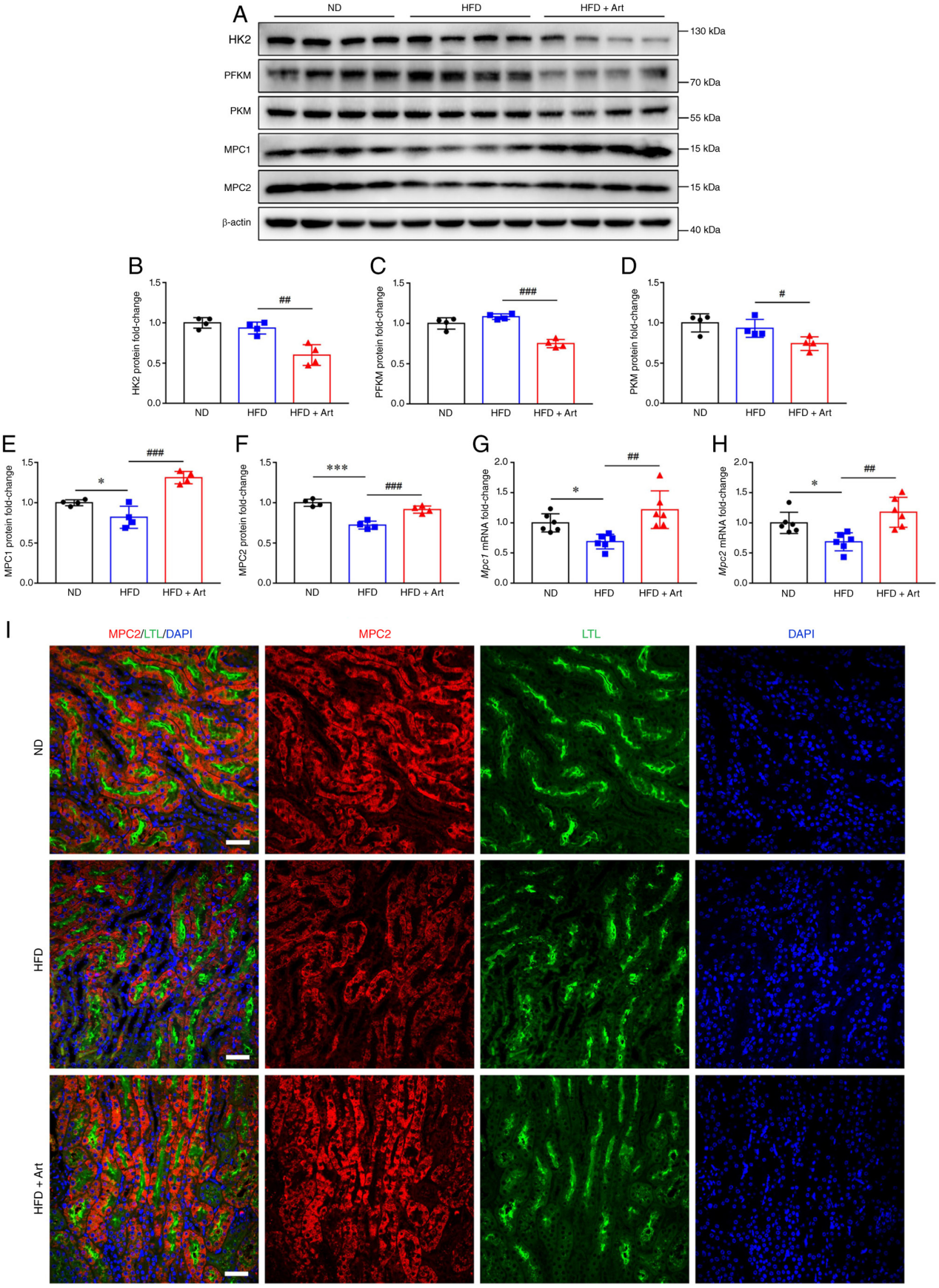



Figure 5. Alterations in the expression of key glycolytic enzymes and MPC1/2 in renal tissue across the three groups, with corresponding analysis of MPC2 distribution within renal tubules. (A) Western blotting images and corresponding semi-quantification of (B) HK2, (C) PFKM, (D) PKM, (E) MPC1 and (F) MPC2 protein levels in renal tissue across the three groups. n=4 per group. The mRNA expression levels of (G) *Mpc1* and (H) *Mpc2* in renal tissue across the three groups. n=6 per group. $^{*}$P<0.05 and $^{***}$P<0.001 vs. the ND group; $^{\#}$P<0.05, $^{\#\#}$P<0.01 and $^{\#\#\#}$P<0.001 vs. the HFD group. (I) Representative fluorescence images showing co-localization of MPC2 and LTL in kidney paraffin sections. Scale bars, 40 $\mu$m. MPC, mitochondrial pyruvate carrier; HK2, hexokinase 2; PFKM, phosphofructokinase, muscle; PKM, pyruvate kinase, muscle; ND, normal diet; HFD, high-fat diet; LTL, lotus tetragonolobus lectin; Art, artemether.

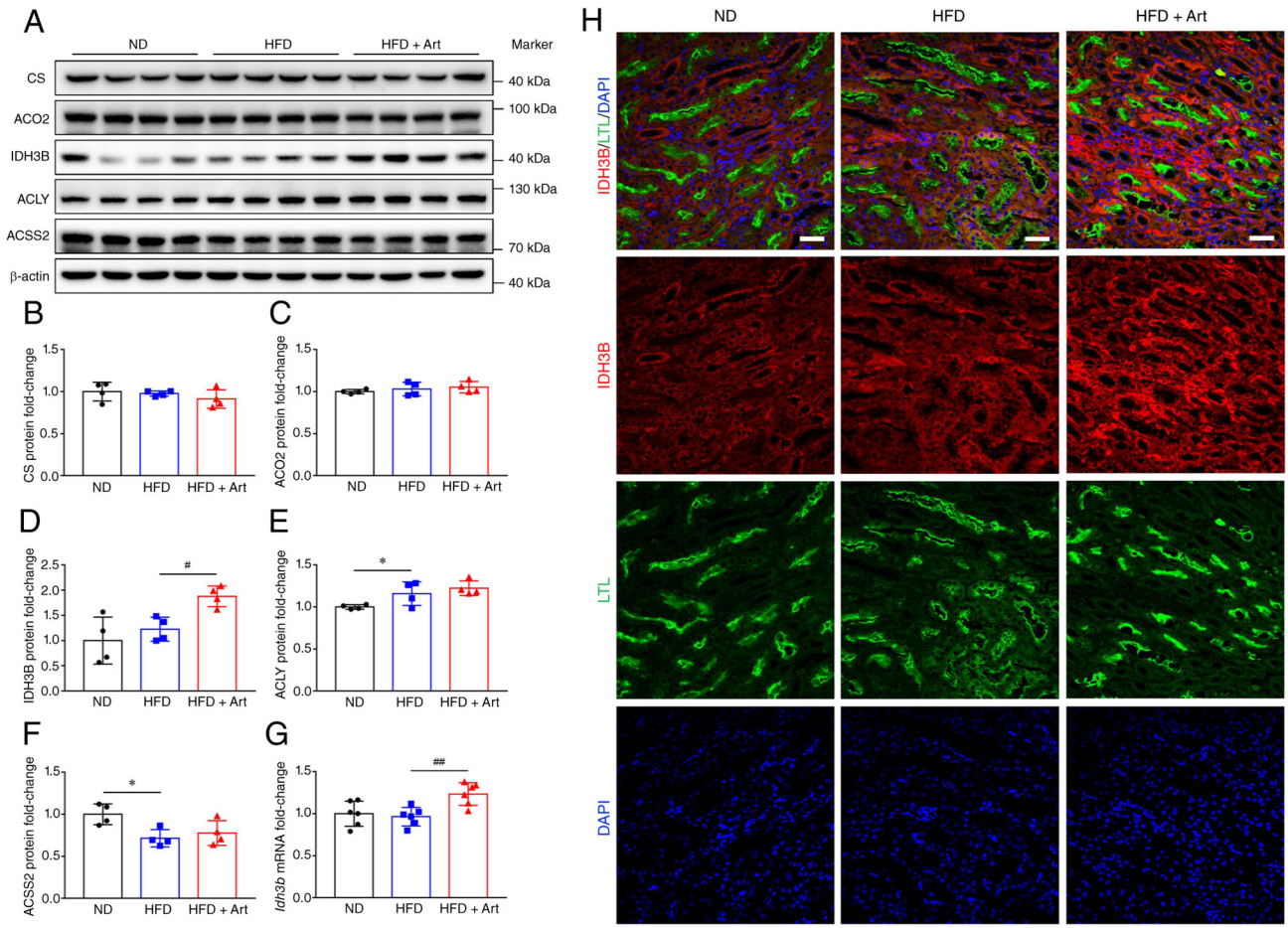



Figure 6. Artemether upregulates the TCA cycle key enzyme IDH3B. (A) Western blotting images and corresponding semi-quantification of (B) CS, (C) ACO2, (D) IDH3B, (E) ACLY and (F) ACSS2 protein levels in renal tissue across the three experimental groups. n=4 per group. (G) Relative mRNA expression of *Idh3b* in renal tissue across the three groups. n=6 per group. $^{*}$P<0.05 vs. the ND group; $^{\#}$P<0.05 and $^{\#\#}$P<0.01 vs. the HFD group. (H) Representative fluorescence images of IDH3B and LTL co-staining in kidney paraffin sections. Scale bars, 40 $\mu$m. TCA, tricarboxylic acid; CS, citrate synthase; ACO2, aconitase 2; IDH3B, isocitric dehydrogenase subunit b; ACLY, ATP citrate lyase; ACSS2, acyl-CoA synthetase short chain family member 2; ND, normal diet; HFD, high-fat diet; LTL, lotus tetragonolobus lectin; Art, artemether.

group, the PA + OA group exhibited markedly lower relative MT-1 fluorescence intensity, which was markedly restored by artemether treatment (Fig. 7B). Representative fluorescence images illustrate the intensity changes across different treatment groups (Fig. 7C).

*Artemether modulates cellular mitochondrial respiration under PA or OA conditions*. For an improved understanding of the respective effects of PA and OA on cellular mitochondrial respiration, the Cell Mito Stress Test, a robust assay for evaluating mitochondrial respiratory function, was assessed (26). The oxygen consumption rate (OCR) and extracellular acidification rate (ECAR) profiles for each group are shown under PA (Fig. 8A and F) or OA (Fig. 8I and N) conditions. Compared with the BSA control group, the PA group exhibited markedly elevated basal OCR (Fig. 8B), unchanged ATP-linked and proton leak OCR (Fig. 8C and D) and markedly decreased spare respiratory capacity (SRC; Fig. 8E). Additionally, markedly increased basal ECAR (Fig. 8G) and slightly increased Δ oligomycin ECAR (Fig. 8H) were detected in the PA group. Artemether intervention markedly reduced basal OCR (Fig. 8B), ATP-linked OCR (Fig. 8C), basal ECAR (Fig. 8G) and Δ oligomycin ECAR (Fig. 8H), while markedly increasing proton leak OCR (Fig. 8D) and SRC (Fig. 8E). Under OA conditions, the OA group showed markedly elevated basal OCR (Fig. 8J) and proton leak OCR (Fig. 8L), unchanged ATP-linked OCR (Fig. 8K) and slightly decreased SRC (Fig. 8M) compared with the BSA group. Basal ECAR (Fig. 8O) and Δ oligomycin ECAR (Fig. 8P) remained unchanged in the OA group. Artemether intervention yielded effects similar to those under PA conditions, markedly reducing basal OCR (Fig. 8J), ATP-linked OCR (Fig. 8K), basal ECAR (Fig. 8O) and Δ oligomycin ECAR (Fig. 8P), while markedly increasing proton leak OCR (Fig. 8L) and SRC (Fig. 8M).

*Effects of artemether on the activity and gene expression of mitochondrial respiratory complexes V (ATP synthase) and IV (cytochrome c oxidase) under PA + OA conditions*. Oxidative phosphorylation stands as the primary biochemical pathway for cellular ATP production. Compared with the BSA group, the PA + OA group showed slightly reduced ATP synthase activity and markedly increased cytochrome *c* oxidase activity (Fig. 9A and B). However, no significant differences were observed in the gene expression of ATP synthase and cytochrome *c* oxidase subunits (Fig. 9C and D). Following artemether intervention, both ATP synthase and cytochrome *c*

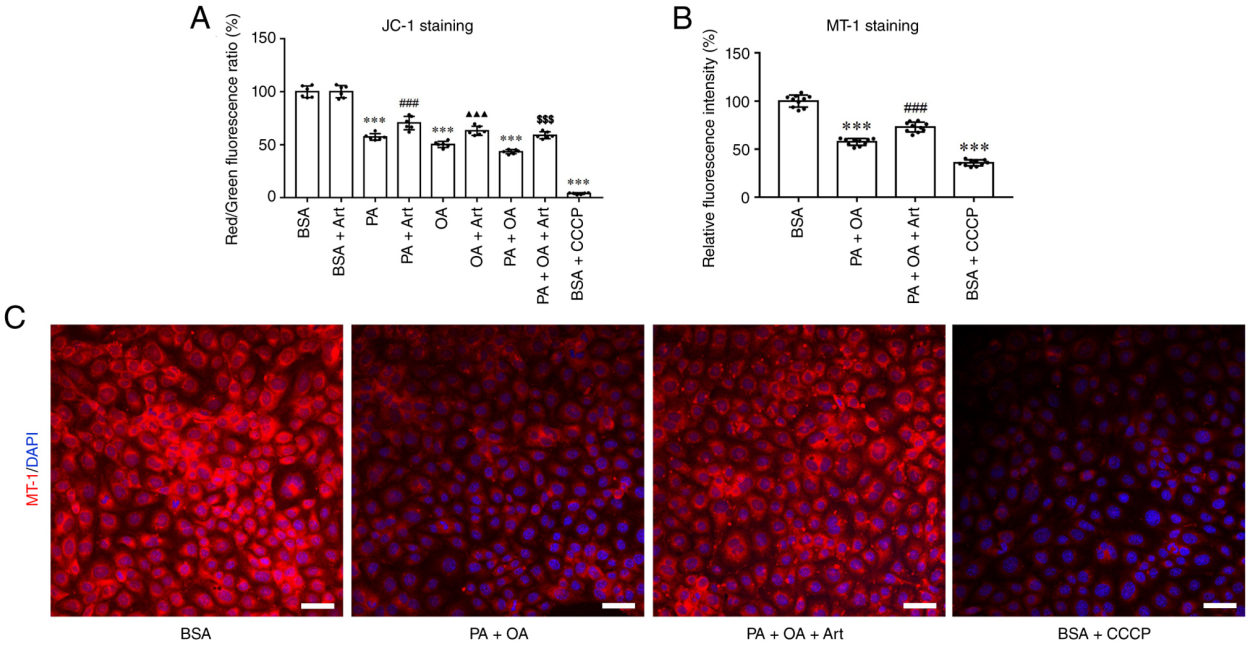



Figure 7. Artemether mitigates MMP reduction induced by PA, OA or PA + OA. (A) MMP assay in TKPTS cells by JC-1 fluorescent dyes. The detailed experimental groups are as follows: BSA (0.25 mM), BSA + Art (0.25 mM + 300 $\mu$M), PA (0.25 mM), PA + Art (0.25 mM + 300 $\mu$M), OA (0.25 mM), OA + Art (0.25 mM + 300 $\mu$M), PA + OA (0.25 mM + 0.25 mM), PA + OA + Art (0.25 mM + 0.25 mM + 300 $\mu$M) and BSA + CCCP positive control group (0.25 mM + 16.7 $\mu$M). n=6 per group. $^{***}$P<0.001 vs. the BSA group; $^{\#\#\#}$P<0.001 vs. the PA group; $^{\blacktriangle\blacktriangle\blacktriangle}$P<0.001 vs. the OA group; $^{\$\$\$}$P<0.001 vs. the PA + OA group. (B) Bar graph showing the MMP changes measured by MT-1 fluorescent dyes in adherent TKPTS cells. The detailed groups are as follows: BSA (0.5 mM), PA + OA (0.25 mM + 0.25 mM), PA + OA + Art (0.25 mM + 0.25 mM + 300 $\mu$M), and BSA + CCCP positive control group (0.5 mM + 16.7 $\mu$M). In each group, 10 fields at x20 objective were selected to calculate the mean fluorescence intensity values. $^{***}$P<0.001 vs. the BSA group; $^{\#\#\#}$P<0.001 vs. the PA + OA group. (C) Representative fluorescence images of MT-1 staining in adherent TKPTS cells from each experimental group. Scale bars, 40 $\mu$m. MMP, mitochondrial membrane potential; PA, palmitic acid; OA, oleic acid; BSA, bovine serum albumin; CCCP, Carbonyl cyanide 3-chlorophenylhydrazone; Art, artemether.

oxidase activities were markedly suppressed (Fig. 9A and B). Correspondingly, artemether treatment also led to marked downregulation of the gene expression of mitochondrial DNA (mtDNA/mt)-encoded subunits: Specifically, *mt-Atp6* and *mt-Atp8* of ATP synthase, as well as *mt-Co1*, *mt-Co2* and *mt-Co3* of cytochrome *c* oxidase (Fig. 9C and D).

*Effects of artemether on lactate excretion and the glycolytic pathway*. Glycolysis is a cytoplasmic metabolic pathway that generates ATP, acting as a vital energy reserve when the efficiency of oxidative phosphorylation declines. As shown in Fig. 10A, lactate excretion in the PA + OA group was slightly higher than that in the BSA group. Changes in the mRNA levels of glycolysis related genes, particularly *Slc2a1* and *Hk2*, were consistent with the pattern of lactate excretion (Fig. 10B). After treatment with artemether, a significant increase in lactate excretion was observed (Fig. 10A). By contrast, the expression of glycolytic enzyme genes was generally downregulated (Fig. 10B). To further explore the regulatory effects of artemether on the glycolytic pathway, the glycolysis stress test was conducted under PA or OA conditions. The ECAR profiles of each group are presented in Fig. 10C and G, under PA and OA conditions respectively. Under PA conditions, no significant differences in glycolysis, glycolytic capacity or glycolytic reserve were detected between the PA group and the BSA group (Fig. 10D-F). In the PA + Art group, basal glycolysis remained unchanged, glycolytic capacity showed a mild decline and glycolytic reserve displayed a significant reduction (Fig. 10D-F). Under OA conditions, compared with the BSA group, the OA group exhibited slightly enhanced glycolysis and glycolytic reserve, accompanied by a marked increase in glycolytic capacity (Fig. 10H-J). Following artemether intervention with OA (OA + Art group), basal glycolysis was slightly elevated, whereas both glycolytic capacity and glycolytic reserve were markedly diminished (Fig. 10H-J).

*Effects of artemether on fatty acid oxidation activity, mitochondrial complex II activity and the expression of genes related to mitochondrial pyruvate oxidation, TCA cycle and TGF-β1 signaling*. Pyruvate dehydrogenase kinase acts as a metabolic brake, which exerts its inhibitory effect by phosphorylating and inactivating the pyruvate dehydrogenase complex. As shown in Fig. 11A, analysis of the gene expression profiles of enzymes involved in mitochondrial pyruvate oxidation revealed that this oxidation process was comparable between the PA + OA and BSA groups. By contrast, artemether treatment appeared to promote mitochondrial pyruvate oxidation. Additionally, fatty acid oxidation activity was evaluated among the three groups. The results indicated that stimulation with PA + OA led to a mild increase in this activity, while intervention with artemether resulted in a significant enhancement (Fig. 11B). Mitochondrial complex II is a unique membrane-bound enzyme that serves as a critical link between the TCA cycle and the electron transport chain (ETC). As shown in Fig. 11C and D, mitochondrial complex II activity and the expression of genes related to the TCA cycle were comparable between the PA + OA and BSA groups.

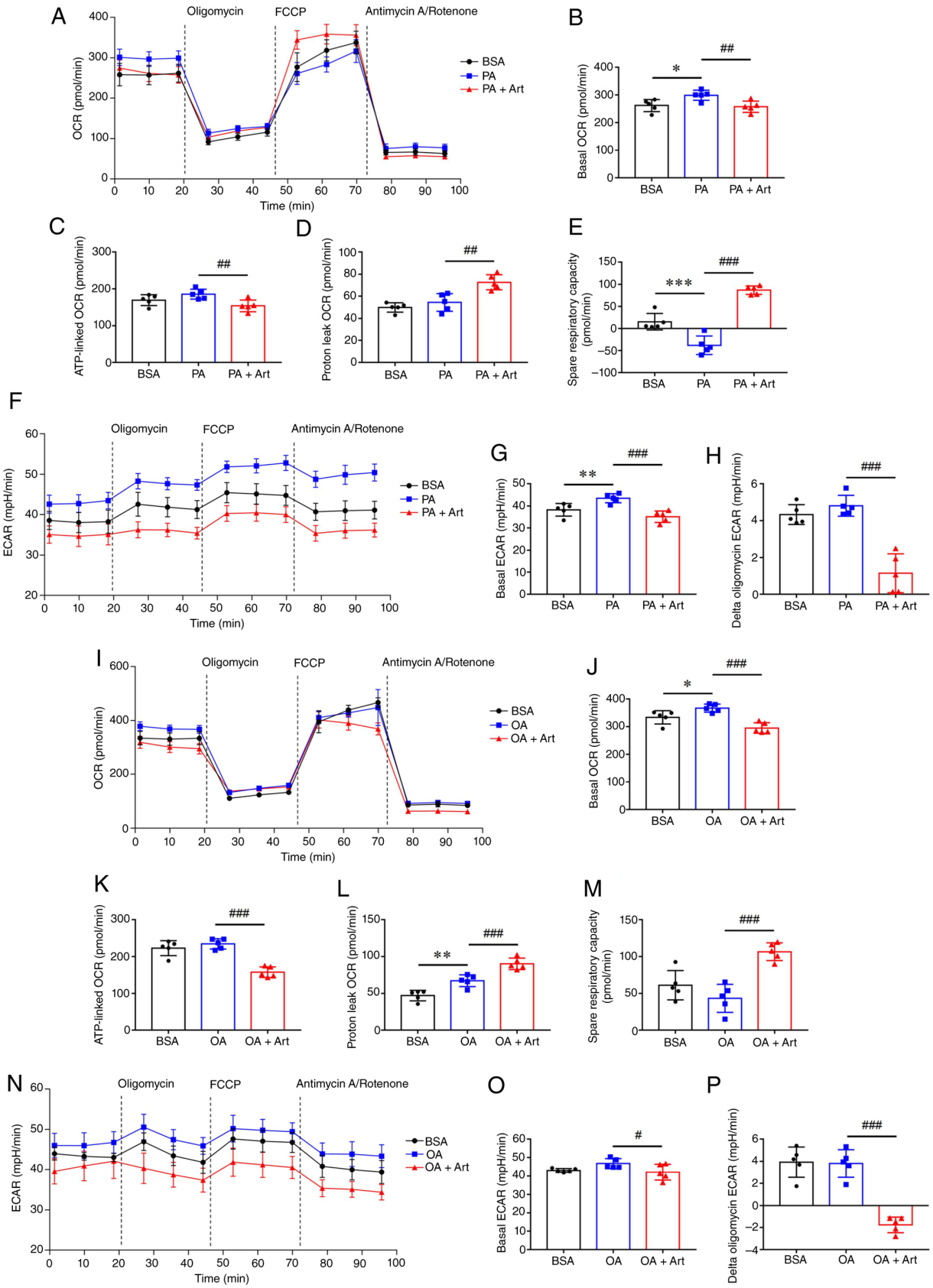



Figure 8. Effects of artemether on Cell Mito Stress Test under PA or OA conditions. (A) The OCR and (F) ECAR curves from different groups under PA conditions. The groups are as follows: BSA (0.2 mM), PA (0.2 mM) and PA + Art (0.2 mM + 300 $\mu$M). Bar graphs showing the (B) basal OCR, (C) ATP-linked OCR, (D) proton leak OCR, (E) spare respiratory capacity, (G) basal ECAR and (H) Δ oligomycin ECAR changes in each group. n=5 per group. $^{*}$P<0.05, $^{**}$P<0.01 and $^{***}$P<0.001 vs. the BSA group; $^{\#\#}$P<0.01 and $^{\#\#\#}$P<0.001 vs. the PA group. (I) The OCR and (N) ECAR curves from different groups under OA condition. The groups are as follows: BSA (0.2 mM), OA (0.2 mM) and OA + Art (0.2 mM + 300 $\mu$M). Bar graphs showing the (J) basal OCR, (K) ATP-linked OCR, (L) proton leak OCR, (M) spare respiratory capacity, (O) basal ECAR and (P) Δ oligomycin ECAR changes in each group. n=5 per group. $^{*}$P<0.05 and $^{**}$P<0.01 vs. the BSA group; $^{\#}$P<0.05 and $^{\#\#\#}$P<0.001 vs. the OA group. PA, palmitic acid; OA, oleic acid; Art, artemether; BSA, bovine serum albumin; OCR, oxygen consumption rate; ECAR, extracellular acidification rate; Art, artemether.

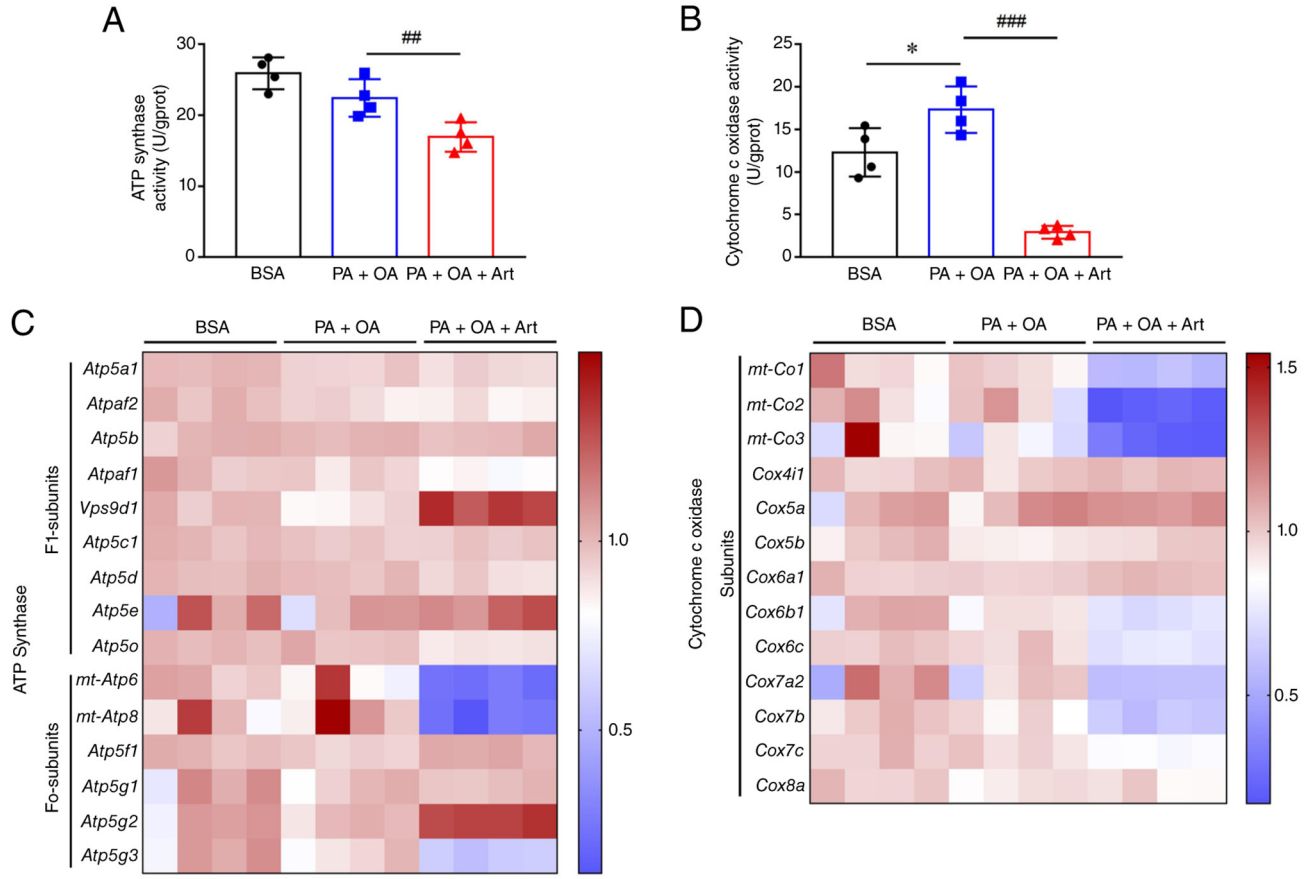



Figure 9. Impact of artemether on the enzymatic activity and subunit gene expression of ATP synthase and cytochrome *c* oxidase under PA + OA condition. Enzymatic activity of (A) ATP synthase and (B) cytochrome *c* oxidase in the three experimental groups. n=4 per group. $^{*}$P<0.05 vs. the BSA group; $^{\#\#}$P<0.01 and $^{\#\#\#}$P<0.001 vs. the PA + OA group. Gene expression of (C) ATP synthase and (D) cytochrome *c* oxidase subunits in each group. PA, palmitic acid; OA, oleic acid; BSA, bovine serum albumin; Art, artemether.

Following artemether treatment, mitochondrial complex II activity was markedly reduced, while the gene expression of TCA cycle enzymes (*Cs*, *Idh3b*, *Ogdhl*, *Dlst*, *Dld*, *Suclg2*, *Sdhb*, and *Mdh2*) was upregulated (Fig. 11C and D). The TGF-β1 signaling pathway serves a pivotal role in the response of PTs to various types of injury, and it can regulate cell growth and proliferation (27). Compared with the BSA group, PA + OA stimulation led to varying degrees of upregulation in the gene expression of *Tgfb1*, *Tgfbr1* and *Tgfbr2* (Fig. 11E). Notably, artemether intervention markedly suppressed the activation of the TGF-β1 signaling pathway (Fig. 11E).

*Effects of artemether on Dgat1 and Dgat2 mRNA expression in renal tissue*. Compared with the ND group, mice in the HFD group exhibited markedly reduced mRNA levels of both *Dgat1* and *Dgat2* in renal tissue (Fig. S1A and B). Artemether treatment partially upregulated the mRNA expression of both genes; however, this increase did not reach statistical significance (Fig. S1A and B).

*Artemether reduces serum TG and TC levels in HFD-induced obese mice*. Compared with the ND group, serum TG levels in the HFD group remained comparable, whereas TC levels were markedly elevated (Fig. S2A and B). Notably, artemether treatment markedly reduced both parameters (Fig. S2A and B).

## Discussion

The present study reported that artemether reduced kidney mass and prevented renal PTs enlargement in long-term HFD mice, without affecting body weight. This effect is likely attributable to the inhibition of PTs proliferation, which is potentially mediated by artemether's modulation of mitochondrial respiration.

Following prolonged HFD induction, mice developed an obese phenotype accompanied by a significant increase in kidney weight. Pathological analysis identified PTs enlargement with increased nuclear counts as the primary morphological alteration. Furthermore, the mRNA expression levels of *Ki-67*, *Tgfb1*, *Tgfbr1* and *Tgfbr2* in renal tissue from each group provided additional evidence supporting these pathological changes. Consistent with abnormally increased TG and TC contents in renal tissue, excessive LD deposition in renal tubules was observed under Oil red O staining in the HFD group. Co-staining of DGAT1 and LTL confirmed that PTs were the prominent sites of LD accumulation. Notably, artemether treatment did not markedly alter the concentrations of TG and TC in renal tissue. These results suggest that the preventive effects of artemether on PTs enlargement may not be achieved through eliminating LDs. In HFD-fed mice, renal *Dgat1* and *Dgat2* mRNA levels were markedly downregulated, which may represent a negative feedback mechanism

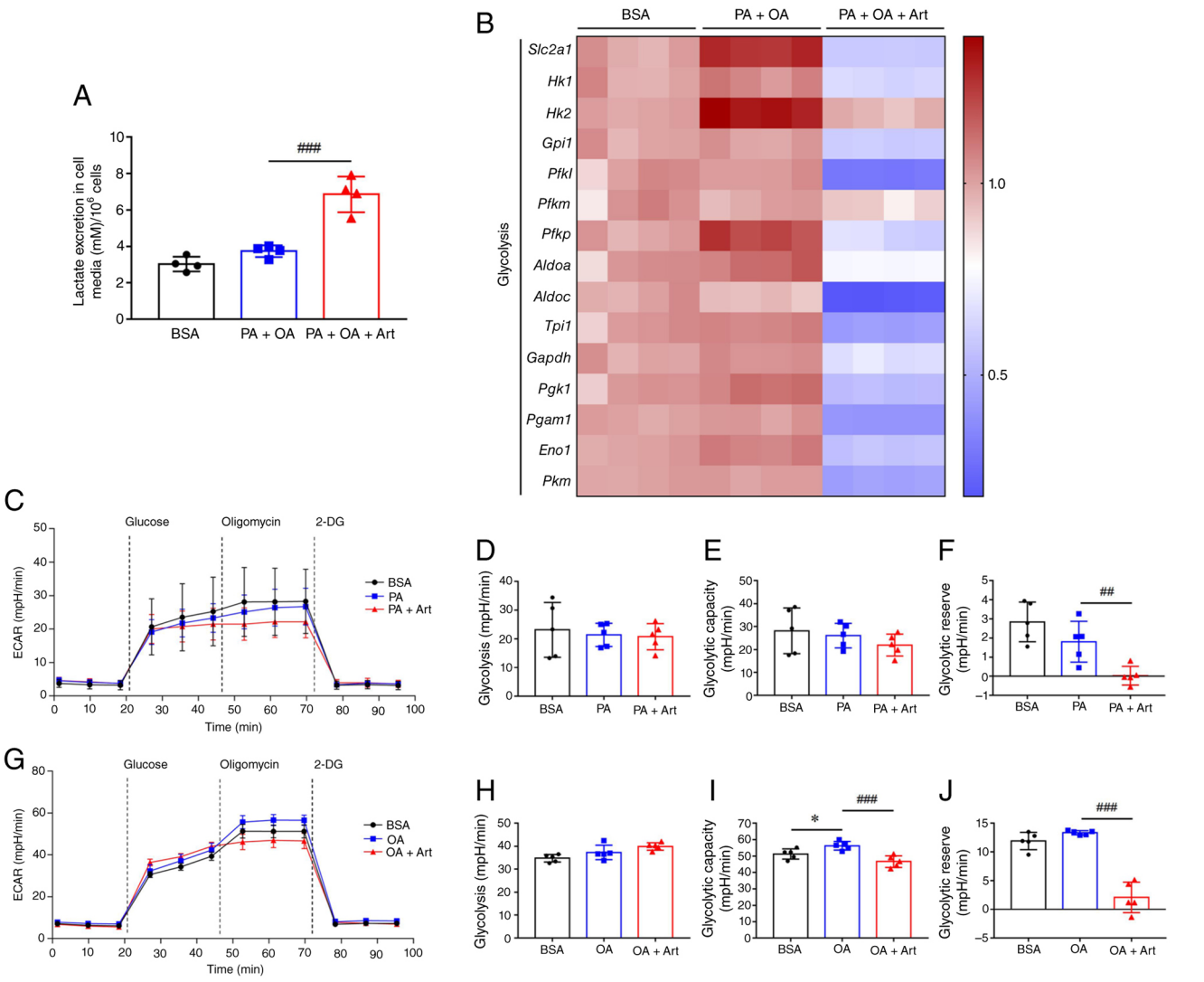



Figure 10. Effects of artemether on lactate excretion and gene expression of glycolytic pathway under PA + OA conditions, and effects of artemether on Glycolysis Stress Test under either PA or OA conditions. (A) Assessment of lactate excretion in cell culture media in the three groups. n=4 per group. ###P<0.001 vs. the PA + OA group. (B) Transcriptional analysis of the glycolytic pathway across the three groups. (C) The ECAR curves of the different experimental groups under PA condition. The groups are as follows: BSA (0.2 mM), PA (0.2 mM) and PA + Art (0.2 mM + 300 $\mu$M). Bar graphs showing the (D) glycolysis, (E) glycolytic capacity and (F) glycolytic reserve changes in each group. n=5 per group. ##P<0.01 vs. the PA group. (G) The ECAR curves of the different experimental groups under OA conditions. The groups are as follows: BSA (0.2 mM), OA (0.2 mM) and OA + Art (0.2 mM + 300 $\mu$M). Bar graphs showing the (H) glycolysis, (I) glycolytic capacity and (J) glycolytic reserve changes in each group. n=5 per group. *P<0.05 vs. the BSA group; ###P<0.001 vs. the OA group. PA, palmitic acid; OA, oleic acid; BSA, bovine serum albumin; ECAR, extracellular acidification rate; Art, artemether.

in response to renal TG accumulation. Although artemether treatment tended to upregulate the expression of these genes, the changes did not reach statistical significance. Regarding systemic lipid profiles, HFD induction led to markedly elevated serum TC levels, whereas serum TG levels remained unaltered. Artemether administration markedly reduced both serum TG and TC concentrations, suggesting its potential to alleviate the systemic lipid burden. However, the correlation between systemic lipid profiles and renal lipid accumulation warrants further investigation.

Cell growth and proliferation are fundamentally dependent on energy metabolism, with highly proliferating cells exhibiting a distinct metabolic program compared with quiescent cells (28). Alterations in the RER revealed that fatty acids serve as the primary systemic energy source in HFD mice and artemether treatment further enhances fatty acid utilization. In the kidneys of HFD mice, renal lipolysis and pyruvate transport into the mitochondrial matrix were impaired, while mitochondrial β-oxidation, glycolysis and the TCA cycle remained unaltered. Results from the HFD + Art group indicated that artemether promotes renal lipolysis, suppresses glycolysis, facilitates pyruvate transport and accelerates the TCA cycle flux in PTs. Notably, the upregulation of *Atgl* mRNA was not accompanied by a significant reduction in renal TG levels. This discrepancy may be attributed to post-translational regulatory mechanisms or the lack of strict dietary control in the HFD + Art group, where continuous lipid intake might have counterbalanced the enhanced lipolysis induced by artemether. Based on the findings of *in vivo* animal studies, it was hypothesized that artemether may suppress the proliferation of PTs in HFD mice by modulating mitochondrial function and metabolic pathways. To further elucidate the underlying mechanisms, *in vitro* experiments were performed.

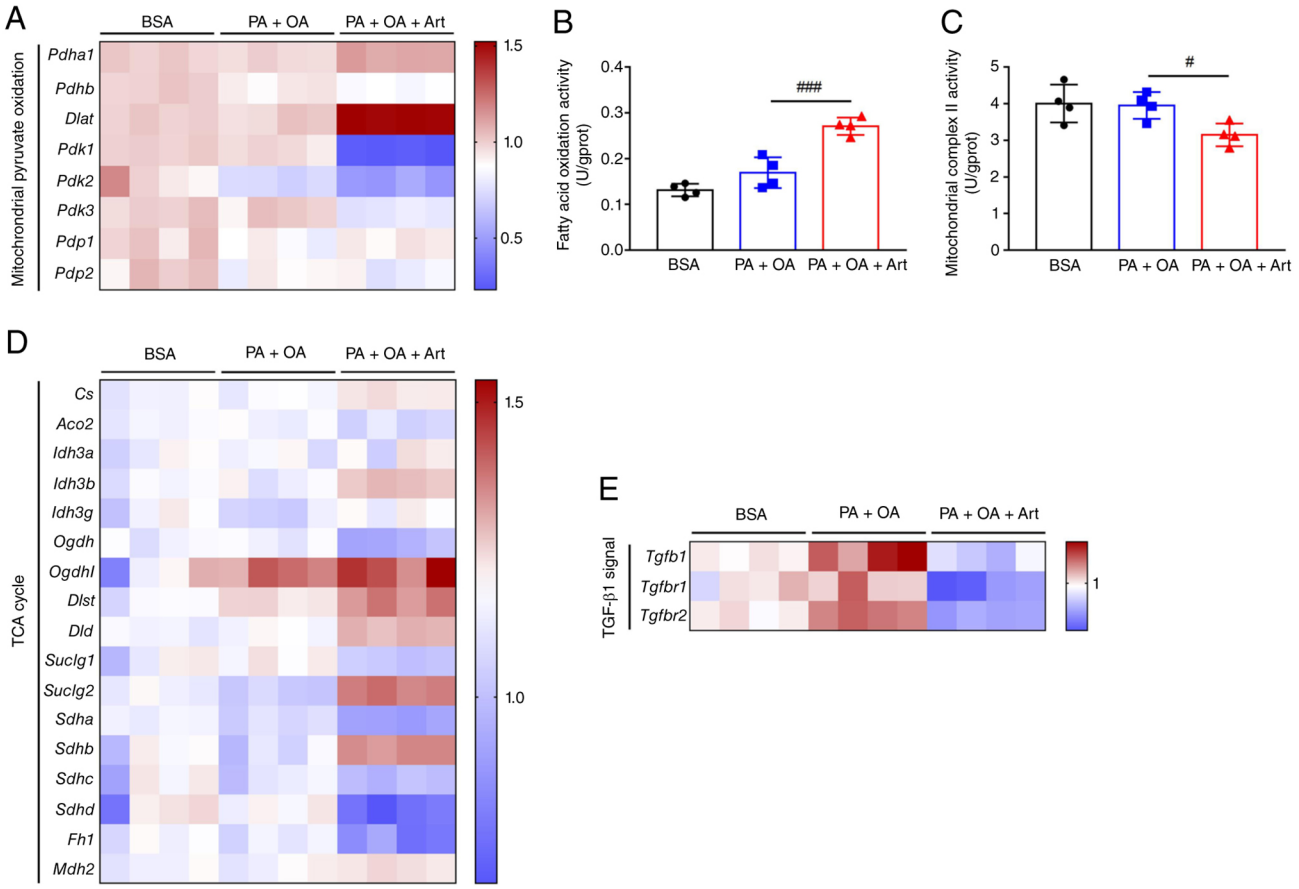



Figure 11. Determination of fatty acid oxidation and mitochondrial complex II activity, and transcriptional analysis of mitochondrial pyruvate oxidation, TCA cycle and TGF-β1 signaling under PA + OA conditions. (A) Gene expression of important enzymes associated with mitochondrial pyruvate oxidation in each group. (B) Activity of fatty acid oxidation and (C) mitochondrial complex II among the three groups. n=4 per group. $^{\#}$P<0.05 and $^{\#\#\#}$P<0.001 vs. the PA + OA group. Transcriptional levels of genes involved in the (D) TCA cycle and (E) TGF-β1 signaling pathway across the three groups. PA, palmitic acid; OA, oleic acid; TCA, tricarboxylic acid; Art, artemether.

MMP serves as the core driving force for ATP synthesis and is implicated in multiple key cellular functions (29). The *in vitro* results demonstrated that artemether can markedly mitigate the decline in MMP after PA, OA or PA + OA stimulation, while not affecting MMP in the BSA group. Using a Cell Mito Stress Test, PA or OA treatment resulted in a significant elevation of basal OCR. Following intervention with artemether, mitochondrial respiration was disrupted, as evidenced by a reduction in ATP-linked OCR, concurrent with increases in proton leak OCR and SRC. Moreover, under the experimental conditions of the Cell Mito Stress Test, artemether markedly decreased both basal ECAR and the oligomycin-induced change in ECAR (Δ oligomycin ECAR). Notably, Δ oligomycin ECAR acts as an indirect biomarker for evaluating the cellular capacity to switch energy metabolism from oxidative phosphorylation to glycolysis. These findings suggested that the biological activity of artemether may be linked to the regulation of oxidative phosphorylation and glycolytic pathways.

ATP synthase and cytochrome *c* oxidase are core components of the oxidative phosphorylation system anchored in the inner mitochondrial membrane. Although no significant differences were detected in mRNA expression levels of subunits belonging to these two complexes between the BSA and PA + OA groups, notable alterations in their enzymatic activities were observed. Specifically, cytochrome *c* oxidase activity was markedly elevated in the PA + OA group, suggesting that fatty acid treatment enhances the function of this terminal oxidase in the mitochondrial ETC. By contrast, ATP synthase activity exhibited only a slight decrease, indicating that the ATP production efficiency of this complex remains largely intact under PA + OA exposure. Following intervention with artemether, the activities of both ATP synthase and cytochrome *c* oxidase were markedly reduced. Concurrently, the transcript levels of *mt-Atp6* and *mt-Atp8* (mtDNA-encoded subunits of ATP synthase), along with *mt-Co1*, *mt-Co2* and *mt-Co3* (mtDNA-encoded subunits of cytochrome *c* oxidase) were markedly downregulated by artemether. Integrating the results from the Cell Mito Stress Test, we hypothesize that the core biological activity of artemether is mediated through the suppression of mitochondrial oxidative phosphorylation.

Glycolysis is also a fundamental biochemical pathway that drives ATP production. It is a rapid process, yet less efficient than mitochondrial oxidative phosphorylation (30). Lactate excretion into the cell culture medium is commonly used to assess glycolytic pathway activity. Under the condition of PA + OA, a mild elevation in lactate excretion into the media, along with significant upregulation of *Slc2a1* and *Hk2* transcript levels, suggested that glycolytic activity was enhanced by fatty acids. Following artemether administration,

a marked increase in lactate excretion was observed, whereas the mRNA expression levels of most glycolytic enzymes were markedly downregulated. Gene expression drops do not always match protein levels and post-translational modifications can activate existing enzymes even as transcription declines. It is conventionally understood that impaired oxidative phosphorylation forces cells to rely on glycolysis for energy production (31), and the concurrent downregulation of glycolysis-associated mRNAs may represent a negative feedback regulation of this pathway.

To further explain these seemingly contradictory observations, glycolysis stress tests under PA or OA conditions were performed separately. The results showed that PA had no significant effect on glycolysis, glycolytic capacity or glycolytic reserve. By contrast, OA markedly enhanced glycolytic capacity, with a concomitant slight increase in both glycolysis and glycolytic reserve. Notably, following artemether intervention, glycolysis remained unchanged, whereas the glycolytic reserve was markedly reduced under both PA and OA conditions. Therefore, it was hypothesized that artemether may force cells to undergo glycolysis by interfering with oxidative phosphorylation, while simultaneously restricting the glycolytic reserve and expression of genes associated with glycolysis. The specific mechanisms remain to be elucidated, but it should be explored in the future.

Mitochondrial pyruvate oxidation and fatty acid oxidation constitute the primary routes for acetyl-CoA production, which fuels the TCA cycle within the mitochondrial matrix. Relative to the BSA group, the PA + OA group exhibited comparable transcript levels of enzymes related to pyruvate oxidation, coupled with a slight elevation in fatty acid oxidation activity. Artemether intervention led to a significant downregulation of *Pdk1*, *Pdk2* and *Pdk3*, suggesting a potential enhancement of mitochondrial pyruvate oxidation. In parallel, fatty acid oxidation activity assay revealed that artemether robustly potentiated this pathway under PA + OA conditions. Mitochondrial complex II is the only enzyme in the TCA cycle that catalyzes the oxidation of succinate to fumarate while transferring electrons to the ETC. No significant differences in mitochondrial complex II activity or in the mRNA expression levels of most other TCA cycle-related enzymes were observed between the BSA and PA + OA groups. Analysis of the transcript levels of TCA cycle enzymes indicates that the TCA cycle rate appeared to be accelerated after artemether treatment, even though mitochondrial complex II activity was markedly decreased. Furthermore, transcript levels of *Tgfb1* and its receptors were upregulated to varying degrees following PA + OA stimulation. Artemether treatment markedly downregulated their transcription, which provides a plausible mechanistic explanation for its inhibitory effect on cell proliferation. Collectively, these findings suggested that artemether initially inhibits basal mitochondrial respiration, as well as the activities of cytochrome *c* oxidase and ATP synthase. In response, cells activate a compensatory feedback mechanism, upregulating fatty acid oxidation, pyruvate oxidation and TCA cycle flux, to preserve energy homeostasis and restore the MMP. The elevated MMP enhances proton conductance, thereby driving proton leak as a means to dissipate this potential. Nevertheless, the precise direct target of artemether, and whether it directly impairs the mitochondrial ETC remain to be elucidated.

The limitations of the present study should be discussed: First, only male C57BL/6 mice were used in the present study. This choice was made because the HFD-induced obesity model has been extensively characterized in males, thereby minimizing biological variability. Female mice are known to be more resistant to the obesogenic effects of a HFD, a phenomenon partly attributed to differences in sex hormones and metabolic profiles (32). Therefore, the therapeutic potential of artemether in female mice remains unknown and should be explored in future research. Second, only a single dose of artemether was evaluated in the present study. This dosage was selected based on previously published evidence demonstrating its therapeutic efficacy in analogous metabolic disease models (33,34). The clinical dosing of artemether varies depending on the formulation (oral vs. injectable) and the patient's age. For the treatment of malaria, the standard dose is 3.2 mg/kg on admission followed by 1.6 mg/kg once daily until oral therapy is tolerated (35). Currently, artemisinin-based combination therapy is recommended as the first-line treatment for malaria, with artemether-lumefantrine being the most widely used combination. Artemether is primarily metabolized by the liver cytochrome P450 (CYP450) system and predominantly eliminated via biliary excretion. Due to minimal renal excretion of the parent drug, artemether poses a low risk of renal toxicity at therapeutic antimalarial doses. Nevertheless, careful monitoring is advised during prolonged high-dose administration, particularly in patients with severe renal impairment (36). Third, potential off-target metabolic effects of artemether in obese patients warrant careful consideration. Due to its high lipophilicity, the expanded adipose tissue mass in obesity may theoretically alter artemether's volume of distribution. Furthermore, obesity is known to modulate the activity and expression of liver CYP450 enzymes (37). As a substrate of the CYP450 system, artemether may undergo altered metabolic clearance in obese individuals, potentially compromising therapeutic efficacy or increasing toxicity. Although it has been reported that artemether-lumefantrine dose modification is not required for overweight and obese patients with malaria (38), the potential for off-target metabolic effects in obesity remains to be fully elucidated.

In summary, the present study demonstrated that artemether reduces kidney weight and prevents PTs enlargement in HFD mice. Crucially, this effect is achieved independently of systemic body weight changes, suggesting a direct reno-protective mechanism rather than a secondary benefit of general weight loss. While current anti-obesity therapies primarily focus on weight reduction, renal structural damage often persists despite weight management. Artemether offers a distinct advantage as an adjunctive therapy that directly targets renal pathology, providing protection even if systemic weight loss is suboptimal. Furthermore, the capacity of artemether to remodel mitochondrial respiration and metabolism suggests that it may have clinical value for kidney diseases associated with metabolic dysfunction.

Future studies should focus on two key areas to further elucidate the mechanism of artemether. First, direct target identification is essential to determine whether artemether

physically interacts with specific ETC components. Techniques such as cellular thermal shift assay, affinity-based pull-down/photoaffinity labeling with an artemether probe, or assays using isolated mitochondria would be useful for this purpose. Second, establishing the causal relationship and functional nature of the observed mitochondrial changes is critical. Time-course experiments comparing the onset of complex activity suppression vs. transcriptional upregulation of substrate-oxidation genes would clarify which change precedes the other. Concurrently, integrating assessment of uncoupling protein expression/proton leak titration and mitochondrial reactive oxygen species levels would help distinguish whether the phenotype reflects protective uncoupling or broader mitochondrial dysfunction.

**Acknowledgements**

Not applicable.

**Funding**

The present study was supported by Sanming Project of Medicine in Shenzhen (grant no. SZZYSM202311004) and Shenzhen Science and Technology Project (grant no. JCYJ20220531092405011).

**Availability of data and materials**

The data generated in the present study may be requested from the corresponding author. The RNA sequencing data generated in the present study may be found in the GEO under accession number GSE317009 or at the following URL: https://www.ncbi.nlm.nih.gov/geo/query/acc.cgi?&acc=GSE317009.

**Authors' contributions**

PH and HS conceived and designed the study. WW performed the majority of the experiments and analyzed most of the data. LS participated in the animal experiments and performed some of the immunoblotting experiments. HL and YZ participated in the animal experiments. XY participated in animal tissue processing and sectioning. MS performed transmission electron microscopy imaging. PH and WW wrote the manuscript. All authors have read and approved the final manuscript. WW, HS and PH confirm the authenticity of all the raw data.

**Ethics approval and consent to participate**

All animal experiments were performed in accordance with the ARRIVE guidelines and approved (approval no. AP0044004) by Animal Ethics Committee of Peking University Shenzhen Graduate School.

**Patient consent for publication**

Not applicable.

**Competing interests**

The authors declare that they have no competing interests.

**References**

1. Furth SL, Colhoun HM, Kanbay M, Kukla A, Lim LL, MacLaughlin HL, Navaneethan SD, Shroff R, Stenvinkel P, Cheung M, *et al*: The relationship between obesity and chronic kidney disease: Conclusions from a Kidney Disease: Improving Global Outcomes (KDIGO) Controversies Conference. Kidney Int 109: 442-464, 2025.
2. Parmaksiz G, Kekec SD, Cengiz ND and Noyan A: The relationship between body mass index and renal length in obese children. Pediatr Nephrol 35: 901-905, 2020.
3. Oxburgh L: Growth control of the kidney. Curr Top Dev Biol 148: 237-263, 2022.
4. Chen JK, Nagai K, Chen J, Plieth D, Hino M, Xu J, Sha F, Ikizler TA, Quarles CC, Threadgill DW, *et al*: Phosphatidylinositol 3-kinase signaling determines kidney size. J Clin Invest 125: 2429-2444, 2015.
5. Kikuchi H, Chou CL, Yang CR, Chen L, Jung HJ, Park E, Limbutara K, Carter B, Yang ZH, Kun JF, *et al*: Signaling mechanisms in renal compensatory hypertrophy revealed by multi-omics. Nat Commun 14: 3481, 2023.
6. Vallon V and Thomson SC: The tubular hypothesis of nephron filtration and diabetic kidney disease. Nat Rev Nephrol 16: 317-336, 2020.
7. Mohandes S, Doke T, Hu H, Mukhi D, Dhillon P and Susztak K: Molecular pathways that drive diabetic kidney disease. J Clin Invest 133: e165654, 2023.
8. Uehara-Watanabe N, Okuno-Ozeki N, Minamida A, Nakamura I, Nakata T, Nakai K, Yagi-Tomita A, Ida T, Ikeda K, Kitani T, *et al*: Direct evidence of proximal tubular proliferation in early diabetic nephropathy. Sci Rep 12: 778, 2022.
9. Deji N, Kume S, Araki S, Soumura M, Sugimoto T, Isshiki K, Chin-Kanasaki M, Sakaguchi M, Koya D, Haneda M, *et al*: Structural and functional changes in the kidneys of high-fat diet-induced obese mice. Am J Physiol Renal Physiol 296: F118-F126, 2009.
10. Lee HJ, Mariappan MM, Norton L, Bakewell T, Feliers D, Oh SB, Donati A, Rubannelsonkumar CS, Venkatachalam MA, Harris SE, *et al*: Proximal tubular epithelial insulin receptor mediates high-fat diet-induced kidney injury. JCI Insight 6: e143619, 2021.
11. Permyakova A, Hamad S, Hinden L, Baraghithy S, Kogot-Levin A, Yosef O, Shalev O, Tripathi MK, Amal H, Basu A, *et al*: Renal mitochondrial ATP transporter ablation ameliorates obesity-induced CKD. J Am Soc Nephrol 35: 281-298, 2024.
12. Yamamoto T: Autophagic stagnation: A key mechanism in kidney disease progression linked to aging and obesity. Clin Exp Nephrol 29: 711-719, 2025.
13. Xia Y, Shi C, Lu J, Zhu Z, Li M, Pan Y, Huang X, Zhang L and Liu A: Artemisinin and Its derivatives from molecular mechanisms to clinical applications: New horizons beyond Antimalarials. Int J Mol Sci 26: 8409, 2025.
14. Wang Y, Han P, Wang M, Weng W, Zhan H, Yu X, Yuan C, Shao M and Sun H: Artemether improves type 1 diabetic kidney disease by regulating mitochondrial function. Am J Transl Res 11: 3879-3889, 2019.
15. Han P, Wang Y, Zhan H, Weng W, Yu X, Ge N, Wang W, Song G, Yi T, Li S, *et al*: Artemether ameliorates type 2 diabetic kidney disease by increasing mitochondrial pyruvate carrier content in db/db mice. Am J Transl Res 11: 1389-1402, 2019.
16. Han P, Zhan H, Shao M, Wang W, Song G, Yu X, Zhang C, Ge N, Yi T, Li S and Sun H: Niclosamide ethanolamine improves kidney injury in db/db mice. Diabetes Res Clin Pract 144: 25-33, 2018.
17. Han P, Cai Y, Wang Y, Weng W, Chen Y, Wang M, Zhan H, Yu X, Wang T, Shao M and Sun H: Artemether ameliorates kidney injury by restoring redox imbalance and improving mitochondrial function in Adriamycin nephropathy in mice. Sci Rep 11: 1266, 2021.
18. Livak KJ and Schmittgen TD: Analysis of relative gene expression data using real-time quantitative PCR and the 2(-Delta Delta C(T)) method. Methods 25: 402-408, 2001.
19. Sivandzade F, Bhalerao A and Cucullo L: Analysis of the mitochondrial membrane potential using the cationic JC-1 dye as a sensitive fluorescent probe. Bio Protoc 9: e3128, 2019.
20. Szrok-Jurga S, Czumaj A, Turyn J, Hebanowska A, Swierczynski J, Sledzinski T and Stelmanska E: The physiological and pathological role of Acyl-CoA oxidation. Int J Mol Sci 24: 14857, 2023.

21. Kanasaki K: The aberrant glycolysis in kidney proximal tubule: Potential therapeutic target for DKD. Kidney Int 104: 1056-1059, 2023.
22. He Z, Zhang J, Xu Y, Fine EJ, Suomivuori CM, Dror RO and Feng L: Structure of mitochondrial pyruvate carrier and its inhibition mechanism. Nature 641: 250-257, 2025.
23. Arnold PK and Finley LWS: Regulation and function of the mammalian tricarboxylic acid cycle. J Biol Chem 299: 102838, 2023.
24. Izzo LT, Trefely S, Demetriadou C, Drummond JM, Mizukami T, Kuprasertkul N, Farria AT, Nguyen PTT, Murali N, Reich L, *et al*: Acetylcarnitine shuttling links mitochondrial metabolism to histone acetylation and lipogenesis. Sci Adv 9: eadf0115, 2023.
25. Tovar-Ferrero O, Rubio J, Zorzano A, Martinez-Corrales G and Liesa M: Measuring mitochondrial membrane potential. EMBO J 44: 7334-7345, 2025.
26. Yoo I, Ahn I, Lee J and Lee N: Extracellular flux assay (Seahorse assay): Diverse applications in metabolic research across biological disciplines. Mol Cells 47: 100095, 2024.
27. Hong Q, Kim H, Cai GY, Chen XM, He JC and Lee K: Modulation of TGF-beta signaling new approaches toward kidney disease and fibrosis therapy. Int J Biol Sci 21: 1649-1665, 2025.
28. Diehl FF, Sapp KM and Vander Heiden MG: The bidirectional relationship between metabolism and cell cycle control. Trends Cell Biol 34: 136-149, 2024.
29. Ahmed Selim N and Wojtovich AP: Mitochondrial membrane potential and compartmentalized signaling: Calcium, ROS, and beyond. Redox Biol 86: 103859, 2025.
30. Kukurugya MA, Rosset S and Titov DV: The Warburg Effect is the result of faster ATP production by glycolysis than respiration. Proc Natl Acad Sci USA 121: e2409509121, 2024.
31. Ma F and Yu W: The roles of lactate and lactylation in diseases related to mitochondrial dysfunction. Int J Mol Sci 26: 7149, 2025.
32. Adam S, Maas SL, Huchzermeier R, Rakateli L, Abschlag K, Hohl M, Liao L, Bartneck M, Teunissen M, Wouters K, *et al*: The calcium-sensing-receptor (CaSR) in adipocytes contributes to sex-differences in the susceptibility to high fat diet induced obesity and atherosclerosis. EBioMedicine 107: 105293, 2024.
33. Rong G, Cai Y, Weng W, Chen Y, Yu X, Shao M, Han P and Sun H: Artemether attenuates renal tubular injury by regulating iron metabolism in mice with streptozotocin-induced diabetes. Am J Transl Res 14: 6095-6106, 2022.
34. Rong G, Weng W, Huang J, Chen Y, Yu X, Yuan R, Gu X, Wu X, Cai Y, Han P, *et al*: Artemether alleviates diabetic kidney disease by modulating amino acid metabolism. Biomed Res Int 2022: 7339611, 2022.
35. Esu EB, Effa EE, Opie ON and Meremikwu MM: Artemether for severe malaria. Cochrane Database Syst Rev 6: CD010678, 2019.
36. Jin Q, Liu T, Chen D, Yang L, Mao H, Ma F, Wang Y, Li P and Zhan Y: Therapeutic potential of artemisinin and its derivatives in managing kidney diseases. Front Pharmacol 14: 1097206, 2023.
37. Krogstad V, Peric A, Robertsen I, Kringen MK, Vistnes M, Hjelmesæth J, Sandbu R, Johnson LK, Angeles PC, Jansson-Löfmark R, *et al*: Correlation of body weight and composition with hepatic activities of cytochrome P450 enzymes. J Pharm Sci 110: 432-437, 2021.
38. Sugiarto SR, Page-Sharp M, Drinkwater JJ, Davis WA, Salman S and Davis TME: Pharmacokinetic properties of the antimalarial combination therapy artemether-lumefantrine in normal-weight, overweight and obese healthy male adults. Int J Antimicrob Agents 59: 106482, 2022.

Copyright © 2026 Weng et al. This work is licensed under a Creative Commons Attribution-NonCommercial-NoDerivatives 4.0 International (CC BY-NC-ND 4.0) License.